DEPARTMENT OF PHYSICS
UNIVERSITY OF JYVÄSKYLÄ
RESEARCH REPORT No. 7/2009

APPLICATIONS OF TUNNEL JUNCTIONS IN LOW–DIMENSIONAL NANOSTRUCTURES

BY
PANU KOPPINEN

Academic Dissertation
for the Degree of
Doctor of Philosophy

To be presented, by permission of the
Faculty of Mathematics and Science
of the University of Jyväskylä,
for public examination in Auditorium FYS-1 of the
University of Jyväskylä on July 31, 2009
at 12 o'clock noon

Jyväskylä, Finland
July 2009

Preface

The work for this Thesis has been carried out at the Department of Physics and Nanoscience Center in the University of Jyväskylä during years 2004–2009.

I would like to thank Professor Ilari Maasilta for being my thesis supervisor during these years and for his excellent ideas regarding different projects presented in this Thesis. I would like to thank especially our present and former group members Dr. Saumyadip Chaudhuri, Mr. Tero Isotalo, Mr. Juhani Julin, Ms. Jenni Karvonen, Mr. Kimmo Kinnunen, Dr. Thomas Kühn, Ms. Minna Nevala, Dr. Lasse Taskinen and Mr. Lasse Väistö for collaboration. In addition, I want to thank persons from outside our group for the inspiring discussions and creating a good athmosphere in the Department of Physics and Nanoscience Center, especially Mr. Tommi Hakala, Dr. Timo Koponen, Mr. Marcus Rinkiö and Dr. Jussi Toppari. In addition, I thank Prof. Markus Ahlskog and Mr. Jarkko Lievonen for the collaboration related to the AFM project. Laboratory engineers Mr. Antti Nuottajärvi and Mr. Tarmo Suppula are acknowledged for their technical support. Dr. Vesa Apaja is acknowledged for technical support pertaining to the computing facilities.

Financial support from Emil Aaltonen foundation, Ellen and Artturi Nyyssönen foundation, Magnus Ehrnrooth foundation, National Graduate School in Materials Physics and Academy of Finland are gratefully acknowledged.

Finally, I would like to thank my relatives and friends for their support and interest in my work, and showing me that there exists life also outside of physics. I am the most grateful to my beloved wife Niina, and want to thank her with all my heart for her love and support, and for standing by me even when I have spent long days, nights and week ends in the lab.

Jyväskylä, July 2009

Panu Koppinen

Abstract

Koppinen, Panu, 1979–
Applications of tunnel junctions in low–dimensional nanostructures
Jyväskylä: University of Jyväskylä, 2009, 140 p.
(Research report/Department of Physics, University of Jyväskylä,
ISSN 0075–465X; 7/2009)
ISBN 978–951–39-3581–8
diss.

This thesis concentrates on studies of AlO_x based tunnel junctions and their feasibility for cooling, thermometry and strain sensing in suspended nanostructures. The main result of the thesis is cooling of one dimensional phonon modes of a suspended nanowire with normal metal–insulator–superconductor (NIS) tunnel junctions. Simultaneous cooling of both electrons and phonons was achieved, and the lowest phonon temperature reached in the system was 42 mK with an initial temperature of $\sim$100 mK. In addition, suspended devices show cooling still at a bath temperature of 600 mK. The observed thermal transport characteristics show, that the heat flow is limited by the scattering of phonons at the bulk–nanowire interface.

The properties of Al–AlO_x–Al tunnel junctions can be improved by thermal annealing in vacuum at 350–450 °C. Annealing treatment will lead to complete stabilization of the junctions, and on increase in both tunneling resistance and charging energy. In addition, the annealing process shows a marked improvement in the tunneling conductance spectrum, indicated by a disappearance of several resonances, which are a fingerprint of either resonant or inelastic tunneling processes caused typically by impurities located in the tunneling barrier. The superconducting gap of Al is not affected, but the supercurrent is reduced, consistent with the increase of tunneling resistance.

Feasiblity of conventional, sub–micron sized Al–AlO_x–Al tunnel junctions in sensing strain, and therefore displacement, is demonstrated in the final chapter of this thesis. Tunnel junctions show a good response to applied strain (gauge factor), which is competitive with existing strain and displacement detectors.

Keywords Thermal annealing, tunnel junction, SINIS refrigeration, SINIS thermometer, strain sensing

Author's address Panu Koppinen
Nanoscience Center
Department of Physics
University of Jyväskylä
Finland

Supervisor Professor Ilari Maasilta
Nanoscience Center
Department of Physics
University of Jyväskylä
Finland

Reviewers Dr. Antti Manninen
Centre for Metrology and Accreditation
MIKES
Finland

Research Professor Antti Niskanen
Technical Research Center of Finland
VTT
Finland

Opponent Professor Francesco Giazotto
NEST CNR–INFM
Scuola Normale Superiore
Italy

List of Publications

B.I. KOPPINEN, P. J., VÄISTÖ, L. M., AND MAASILTA, I. J., *Complete stabilization and improvement of the characteristics of tunnel junctions by thermal annealing*. Appl. Phys. Lett. **90** (2007) 053503.

B.II. KOPPINEN, P. J., KÜHN, T., AND MAASILTA, I. J., *Effects of charging energy on SINIS tunnel junction thermometry*. J. Low Temp. Phys. **154** (2009) 179–189.

B.III. KOPPINEN, P. J., AND MAASILTA, I. J., *Cooling of suspended nanostructures with tunnel junctions*. J. Phys.:Conf. Series **150** (2009) 012025.

B.IV. KOPPINEN, P. J., AND MAASILTA, I. J., *Cooling of nanomechanical beams with tunnel junctions*. Phys. Rev. Lett. **102** (2009) 165502.

B.V. KOPPINEN, P. J., LIEVONEN, J. T., AHLSKOG, M. E., AND MAASILTA, I. J., *Tunnel junction based displacement sensing for nanoelectromechanical systems*. J. Phys.:Conf. Series **92** (2007) 012051.

B.VI. KOPPINEN, P. J., LIEVONEN, J. T., AHLSKOG, M., AND MAASILTA, I. J., *Strain sensing with sub–micron sized Al–AlO_x–Al tunnel junctions*. Submitted for publication, arXiv:0906.4234.

The author of this Thesis has written, made experiments and data analysis for all papers I.–VI. The author has a major contribution in designing the experimental setup for annealing, used in paper I. In addition, the author has made all samples presented in publications II.–VI. All numerical simulations used in papers IV. and VI. and numerical calculations for thermometry without charging effects in paper II. were made by the author.

Other publications to which the author has contributed

I. GLOOS, K., KOPPINEN, P. J., AND PEKOLA, J. P., *Properties of native ultrathin aluminium oxide tunnel barriers*. J. Phys.:Condens. Matter **15** (2003) 1733–1746.

II. SAVOLAINEN, M., TOUBOLTSEV, V., KOPPINEN, P., RIIKONEN, K.-P., AND ARUTYUNOV, K., *Ion beam sputtering for progressive reduction of nanostructures dimensions*. Appl. Phys. A **79** (2004) 1769–1773.

III. KOPPINEN, P. J., KARVONEN, J. T., TASKINEN L. T. AND MAASILTA, I. J., *Thermal Conduction in Nanostructures by Virtual Photons*. AIP Conf. Proc. **850** (2006) 1556–1557.

IV. KOPPINEN, P. J., VÄISTÖ, L. M. AND MAASILTA, I. J., *Effects of Annealing to Tunnel Junction Stability*. AIP Conf. Proc. **850** (2006) 1639–1640.

Contents

Chapter 1

Introduction

Typically, physical systems that exist in nature are three dimensional. However, dimensions of a system can be artificially reduced to two, one or even zero by using modern micro and nanofabrication techniques. The system can be considered to be low–dimensional for some particle species, such as electrons or phonons, if they are confined in space. For example, particles in two dimensional systems are restricted to move in plane, in one dimensional systems in wire, and in zero dimensional systems particles are fully localized.

During the last two decades, the experimental studies of low dimensional nanostructures have been mainly concentrated on electron systems, such as two dimensional electron gas (2DEG). For example, experimental realization of 2DEG can be made out of semiconductor heterostructures [1]. Furthermore, the dimensionality of electrons in 2DEG can be reduced to one dimensional wires or zero dimensional quantum dots with external gate electrodes. Several new phenomena, such as fractional quantum Hall effect in 2DEGs, quantized electrical conductance in ballistic quantum point contacts and zero dimensional systems behavior as artificial atoms have been observed in low dimensional electron systems [1].

In addition to electron transport, also heat transport is affected by the low dimensionality: for example, thermal conductance is quantized in similar manner as electric conductance in one dimensional electron gases. The quantization of thermal conductance has been demonstrated for one dimensional phonon system [2], and also more recently for thermal photons [3]. Also the effects of phonon dimensionality to interaction between electrons and phonons has been experimentally observed [4]. Understanding and controlling of the heat transport phenomena in low–dimensional systems can open a new era for ultrasensitive bolometry and calorimetry [5], where the sensitivity of a detector is enchanced by the weakness of thermal coupling to its environment. In addition, the understanding and control of heat flow mechanisms would be beneficial for the quantum computing applications, since

thermal coupling to the heat bath is one origin of dephasing.

For low–dimensional phonon systems, the confinement cannot be achieved by simply applying some external potential, as in the case of electrons, but mechanically suspended structures are needed to decouple the low–dimensional and the bulk modes. The suspended structures can be used as nanoelectromechanical systems (NEMS), which contain mechanical system coupled to electrical transducers. Probably one of the most exciting goals of current NEMS research is to reach a quantum limited motion [6], since it would provide an excellent laboratory to study quantum mechanics as well as offer an opportunity to improve the sensitivity of mechanical detectors for displacement [7,8], force [9] and mass sensing [10]. To achieve the quantum limit of a mechanical system, would require to cool it down to the mechanical ground state, which typically means temperature below 100 mK.

One category of electrical nanostructures that can be employed in low-dimensional systems for example in cooling, thermometry and displacement sensing are tunnel junctions. To date, tunnel junctions are widely used in applications of nanoelectronics, such as radiation detectors [11], thermometers and coolers [12], magnetometers (SQUIDS) [13] and single electron transistors [14], just to name a few. In addition, magnetic tunnel junctions are developed for the memory applications [15] and the applicability of superconducting tunnel junctions for solid state realization of a quantum bit has been widely studied [16].

This thesis concentrates on studies of AlO_x based tunnel junctions and their feasibility for applications such as cooling [III, IV], thermometry [II], and strain and displacement sensing in low–dimensional suspended nanostructures [V, VI]. In addition, a novel method to improve the characteristics of tunnel junctions by vacuum thermal annealing is presented [I].

Chapter 2

Properties of tunnel junctions

This chapter of the thesis contains a description of tunnel junctions, normal–normal, normal–superconductor and Josephson tunneling is introduced as well. Also the fabrication of junctions and the influence of thermal annealing in vacuum on tunnel junction characteristics is presented.

Tunnel junctions used in this thesis contained metallic electrodes (either aluminium or copper) separated by a thin (∼1–2 nm thick) insulating aluminium oxide (AlO_x) tunnel barrier. Classically this structure is not able to carry current, but when the insulator is thin enough, the current is carried through the junction by quantum mechanical tunneling of electrons between electrodes. Tunnel junction based devices are widely used in applications of nanoelectronics and the possibility of their use as a solid state realization of quantum bits is being studied, as discussed in the introduction.

2.1 Fabrication of tunnel junctions

Sub–micron sized structures are most easily fabricated with electron beam lithography (EBL) and vacuum evaporation techniques. In this thesis, submicron sized structures fabricated on bulk had either silicon oxide (SiO_x) (publication I.) or silicon nitride (SiN) (publications II.–VI.) as substrate material. Silicon oxide was either grown by thermal oxidation of silicon or by plasma enchanced chemical vapor deposition (PECVD). SiN was low–pressure CVD (LPCVD) grown on top of Si to obtain low–stress films.

To fabricate structures containing tunnel junctions, a double layer of electron beam sensitive resist was used. The first layer consisted of polymethylmethacrylate methacrylic acid (P(MMA-MAA)) in either acetic acid or ethyl lactate and the second layer of polymethylmethacrylate (PMMA) in either anisole or chlorobenzene. The

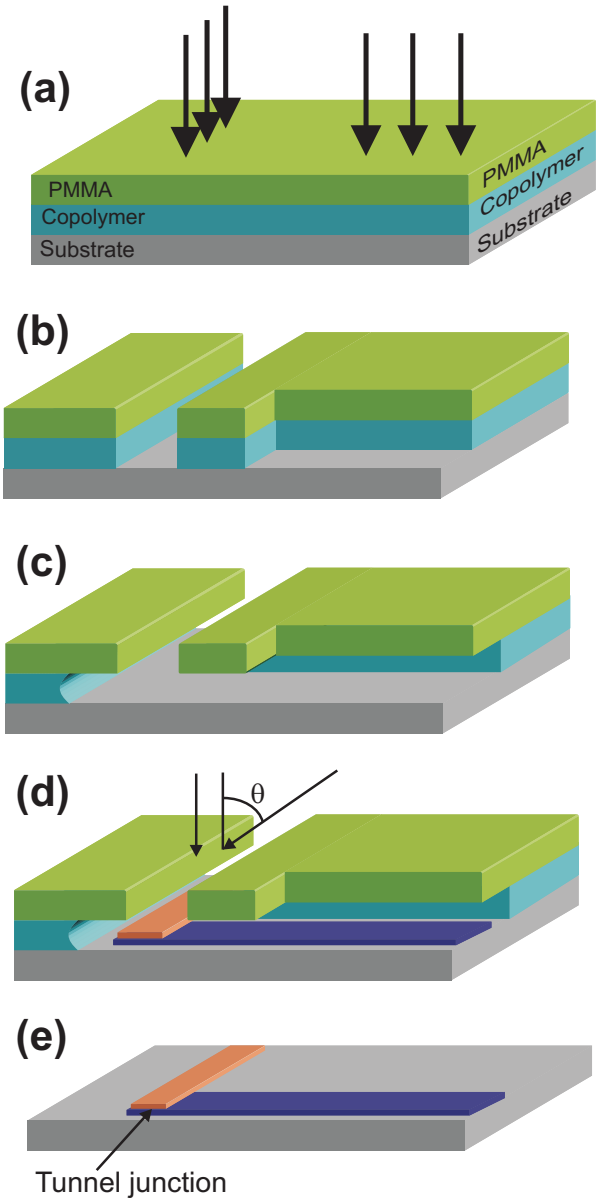

FIGURE 2.1 Schematic view of double angle evaporation process to fabricate tunnel junctions. (a) Electron beam exposure, (b) 1st developer, (c) 2nd developer, (d) metallization from two angles, (e) lift-off.

molecular weight of resist was 950 kDa. Both resists are electron beam sensitive and are called positive resists: Beam of electrons breaks the bonds in the polymer and the exposed area can then be easily removed with developer (Fig. 2.1 (a)). The first layer of resist is called co–polymer and it is more sensitive to e–beam than the top layer, therefore this co–polymer serves as a sacrificial layer to obtain a proper undercut for multiangle evaporation schemes. Typical resist thicknesses were $\sim$300 nm for each layer, obtained by spin coating of the chip with spin speeds of 4000 rpm and 2000 rpm for 50 seconds for bottom and top layers, respectively. After spinning, each layer was baked for 3 minutes at 170 °C.

Pattern design was made with CAD sofware and actual pattering performed in a scanning electron microscope (SEM) equipped with a beam blanker. Samples in publication I. were made with JEOL JSM840A SEM and samples in publications II.–VI. with Raith E–line electron beam writing tool. EBL was followed by a developing step, where samples were developed first with mixture of methyl isobutyl ketone (MIBK) and isopropanol (IPA) with a volume ratio of 1:2 for 45 seconds and then with developer containing 2–methoxyethanol and methanol 1:2 for 6–10 seconds. The first developer reacts with both resist layers (Fig. 2.1 (b)), while the second one has good selectivity between resists and it mainly develops the bottom layer, creating a proper undercut (Fig. 2.1 (c)). The developing process is stopped by rinsing the sample with IPA and blow drying with helium (He) or nitrogen (N_2) gas.

After developing, the samples were cleaned with oxygen plasma in a reactive ion etcher (RIE) to reduce the amount of organic impurities on the substrate surface. Typical parameters for plasma cleaning were 30 W of RF–power, 50 sccm oxygen flow, 0.053 mbar of pressure and a duration of 30 seconds. The plasma cleaning has a significant effect on the quality of tunnel junctions, as discussed later in section 2.6 in this chapter.

Plasma cleaning was followed by deposition of the metal films in either Balzers e–beam evaporator or in an ultra–high vacuum (UHV) chamber equipped with an electron gun. Base pressures of the evaporators were $\sim 10^{-6}$ mbar and $\sim 10^{-9}$ mbar, respectively. Sample stages in both evaporators can be rotated with respect to both horizontal and tilt angles by 360°.

Tunnel junctions studied in this work were based on aluminium oxide (AlO_x) barriers. To make a tunnel junction, first a thin layer of aluminium (Al) is evaporated and then oxidized *in situ* without breaking the vacuum. Typical oxidation pressures ranged from 0.1 mbar to 40 mbar, depending on the application. Deposition of aluminium film was followed by deposition of the other electrode material, either copper (Cu) or another layer of Al from another angle. A schematic picture of the double angle evaporation technique is shown in Fig. 2.1 (d).

The last step in tunnel junction fabrication is lift–off, where the residual resist is removed by immersing the chip in heated acetone, Fig. 2.1 (e). After lift–off, the sample is rinsed with IPA and blow dried with a flow of He gas.

Instead of resists, mechanical masks can be used for multi–angle evaporation. However, the spacing between mask and substrate is typically several microns and therefore the distance between lines becomes easily relatively large even with evaporation from small angles. Tunnel junctions made with a mechanical mask, fabricated from a silicon nitride (SiN) membrane are used e.g. in references [17,18].

2.2 Normal metal–insulator–normal metal tunneling

Tunneling current through a normal metal–insulator–normal metal (NIN) tunnel junction can be written as a function of bias voltage V and temperature T as [19]

$$I(V,T) = \frac{2\pi Ae}{\hbar}\int_{-\infty}^{\infty}\tau(E)N_1(E-eV)N_2(E)[f(E-eV,T)-f(E,T)]\mathrm{d}E \qquad (2.1)$$

where A is the junction area, $\tau(E)$ is the tunneling probability, $N_1(E-eV)$and $N_2(E)$ are density of states (DOS) on metal electrodes and $f(E)$ is the Fermi–Dirac distribution. Tunneling probability, and hence also tunneling current depends exponentially on the barrier parameters: height ϕ_0 and thickness d.

If low temperatures and low bias voltages over the barrier are assumed, only tunneling of electrons at the Fermi–level of the electrodes is taken into account. Then the DOS and the tunneling probability $\tau(E)$ can be treated as constant in energy, and therefore the tunneling current can be written in the form

$$I(V,T) = \frac{1}{eR_T}\int_{-\infty}^{\infty}[f(E-eV,T)-f(E,T)]\mathrm{d}E \qquad (2.2)$$

leading to linear current–voltage (I–V) characteristics with the tunneling resistance $R_T \equiv (2\pi Ae^2\tau(0)N_1(0)N_2(0)/\hbar)^{-1}$. At higher bias voltages, the shape of the tunneling barrier is distorted by the electric field and the tunneling probability can not be taken to be constant, but is a function of energy. The simplest approximation of the barrier is trapezoidal shape, Fig. 2.2. Furthermore, assuming that direct tunneling processes dominate and the tunneling conductance can be written with the help of Wentzel–Kramers–Brillouin (WKB) [20] approximation, the conductance has the form [19,21]

$$G = G_0\left[1+\left(\frac{V}{V_0}\right)^2\right] \qquad (2.3)$$

where $G_0 = e^2 A\sqrt{2m\phi_0}/(h^2 d)\exp(-2d\hbar^{-1}\sqrt{2m\phi_0})$ and $V_0^2 = 4\hbar^2\phi_0/(e^2 m d^2)$, m is the electron mass, h Planck's constant and $\hbar = h/(2\pi)$. This parabolic dependence on the bias voltage is next to the leading order approximation of the tunneling conductance with respect to the applied bias voltage. Result (2.3) can be used for estimating the barrier parameters, and this very simple picture is used as the basis in analyzing normal state tunnel junctions in publication I. However, more accurate modelling of tunnel junctions requires taking into account the effect of image forces, that distort the barrier [21, 18]. The barrier thickness d in the equations above is the effective thickness, related to the physical oxide thickness d_{ox} via relation $d = (m^*/m)^{1/2} d_{\mathrm{ox}}$, where m^* is the effective mass of an electron in the barrier. The relation for effective thickness can be derived from the tunneling current equation (2.1) by using the fact that the prefactor of the integral contains the electron mass in a metal, while the tunneling probability $\tau(E)$ has an effective mass m^* due to the band–structure of an oxide barrier. The band–structure calculations yield $m^*/m = 0.4$ [22] for bulk Al_2O_3 and measured values with ballistic electron emission spectroscopy show $m^*/m = 0.75$ for thin AlO_x [23].

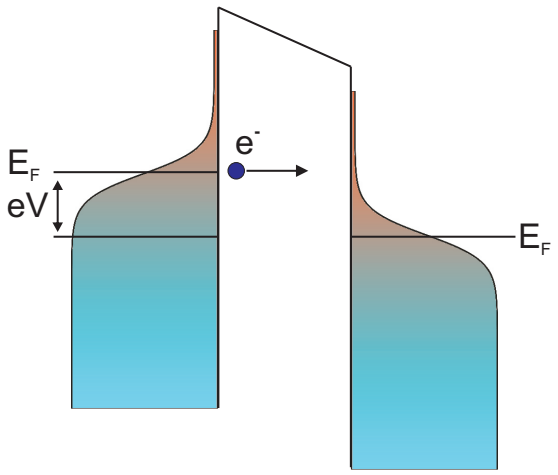

FIGURE 2.2 Schematic view of trapezoidal barrier due to voltage bias eV over the tunnel junction.

2.3 Tunnel junctions in weak Coulomb blockade regime

A tunnel junction consists of two metal electrodes separated by a thin insulating layer, therefore it also has capacitance. The capacitance of a lateral tunnel junction $C = \epsilon\epsilon_0 A/d$, where ϵ is the dielectric constant of an insulating barrier, ϵ_0 electric

constant (vacuum permittivity), A junction area and d barrier thickness. Charging energy for a single electron of an island separated from the rest of the circuit with two tunnel junctions can be written in the form

$$E_C = \frac{e^2}{2C_\Sigma} \,, \tag{2.4}$$

where $C_\Sigma = 2C + C_0$, where C is the junction capacitance and C_0 is the island capacitance to the ground. However, typically C_0 term can be neglected for small islands. Small dimensions of the junction (A $\sim$100 nm$\times$100 nm, d $\sim$1 nm) lead to typical capacitances of the order of fF, and therefore the associated charging energy can easily be order of one kelvin (86 μeV). Hence, at low temperatures the single electron charging effects become significant, leading to Coulomb blockade [14] of the electric current at voltage biases $V < e/C_\Sigma$.

In the weak Coulomb blockade regime $E_C < k_B T$, charging effects are smeared out by temperature, and in systems containing two junctions the tunneling conductance shows a dip around zero voltage bias. The shape of the tunneling conductance obeys a bell–shaped curve [24]

$$G(V) = G_T \left[1 - \frac{2E_C}{k_B T} g\left(\frac{eV}{2k_B T} \right) \right] \tag{2.5}$$

where $G_T \equiv R_T^{-1}$ and $E_C = e^2/(2C_\Sigma)$, and $g(x) = [x\sinh(x) - 4\sinh^2(x/2)]/[8\sinh^4(x/2)]$. The relative depth of the dip is [24]

$$\frac{\Delta G}{G_T} = \frac{E_C}{3k_B T} \,. \tag{2.6}$$

2.4 Normal metal–insulator–superconductor (NIS) tunneling

When one of the electrodes in the tunnel junction is superconducting, the low bias current–to–voltage characteristics change drastically due to the energy gap Δ of superconductor. DOS in a superconductor at weak–coupling limit can be written according to BCS (Bardeen–Cooper–Schrieffer) theory as [25]

$$n_S(E) \equiv \frac{N_s(E)}{N(0)} = \begin{cases} \frac{|E|}{\sqrt{E^2 - \Delta^2}} & , |E| > \Delta \\ 0 & , |E| < \Delta \end{cases} \tag{2.7}$$

where $N(0)$ is the DOS in the normal metal and N_S in the superconductor. Furthermore, the tunneling current in NIS junction can be written in the form

$$I = \frac{1}{eR_T}\int_{-\infty}^{\infty} n_S(E)\left[f_N(E-eV) - f_S(E)\right]\mathrm{d}E\,, \tag{2.8}$$

where f_N and f_S are the Fermi distributions of the normal metal and the superconductor, respectively. Zero temperature limit ($T = 0$) of tunneling current can be calculated analytically, and at bias voltages $V \geq \Delta/e$ it is $I = R_T^{-1}\sqrt{V^2 - (\Delta/e)^2}$, i.e. tunneling current is asymptotically approaching the normal state current (2.2) at high bias voltages.

Tunneling current presented with the above equation shows a sharp cut–off at bias voltage $V = \Delta/e$ leading to zero current in the gap due to the DOS in Eq. (2.7). The DOS in Eq. (2.7) holds exactly for an ideal superconductor. However, real superconductors show broadening of the DOS due to finite life–time effects [26, 27, 28]. Finite life of quasiparticles will lead into broadening of the DOS, according to energy time uncertainty $\delta E = \hbar/\tau$, with τ being the life–time of a quasiparticle in a superconductor. Life–time broadenened DOS can be parametrized with $\Gamma = \delta E$, and written in the form

$$n_S(E) = \left|\mathrm{Re}\left\{\frac{E + i\Gamma}{\sqrt{(E+i\Gamma)^2 - \Delta^2}}\right\}\right|. \tag{2.9}$$

The broadening parameter Γ depends strongly on the quality of evaporated films [27] and is typically of the order $\Gamma/\Delta \sim 2 \times 10^{-4}$ for evaporated Al films used in experiments in this thesis, consistent with values reported by other groups [26, 28, 29]. For niobium (Nb) films however, even two orders of magnitude larger Γ/Δ values have been reported [30]. Life–time broadening effects lead to a finite sub–gap current of a NIS junction, and therefore cause e.g. excess heating in NIS based coolers. More discussion about effects on applications in thermometry and cooling can be found in chapter 3 of this thesis. In addition to life–time broadening, there exist other mechanisms, such as pinholes in the oxide and higher order processes, like Andreev reflection [31, 32] that can lead to finite sub–gap current. However, in this thesis we concentrate only on single electron current in NIS junctions and all data is analyzed by using relation (2.9).

2.5 Josephson junctions

When both electrode materials are superconducting (SIS), the tunnel junction is called a Josephson junction. However, there are other types of Josephson junctions as well consisting of a superconducting weak link or a short normal metal island between superconductors instead of an insulating barrier [25]. In general, all Josephson junctions contain two superconductors that are separated from each other and this separation determines the strength of the coupling between the superconducting electrodes.

According to Ginzburg–Landau theory [25], both superconductors can be characterized by an order parameter $|\Psi|e^{-i\phi_j}$ ($j = 1, 2$) with amplitude $|\Psi|$ and phase ϕ. Coupling, i.e. overlapping of the order parameters between superconductors leads to current at zero–bias voltages [25]

$$I_S = I_c \sin(\Delta\phi) \,, \tag{2.10}$$

where I_c is the critical current and $\Delta\phi \equiv \phi_1 - \phi_2$ is the phase difference between the two superconductors. This is called the DC–Josephson effect and was first predicted by Brian Josephson in 1962 [33]. Furthermore, there exists also an AC–Josephson effect, which shows that if a finite voltage is applied across the junction, the phase difference of the order parameter will evolve in time as

$$\frac{\mathrm{d}(\Delta\phi)}{\mathrm{d}t} = \frac{2eV}{\hbar} \,, \tag{2.11}$$

leading to an alternating current accross the junction with amplitude I_c and frequency $2eV/\hbar$. The phase difference in the superconductor leads to a change in the free energy of the system [25]. The free energy stored in the Josephson junction due to this phase difference is the work done by a current source in changing the phase [25]

$$W = \int V I_S \mathrm{d}t = \text{constant} - E_J \cos(\Delta\phi) \,, \tag{2.12}$$

where the Josephson coupling energy related to the junction is

$$E_J = \frac{\hbar I_c}{2e} \tag{2.13}$$

For tunnel junctions, the relation between tunneling resistance and critical current can be written by the Ambegaokar–Baratoff relation [34, 25]

$$I_c R_T = \frac{\pi\Delta}{2e} \tanh\left(\frac{\Delta}{2k_B T}\right) \,. \tag{2.14}$$

Josephson junctions can be described by the resistively and capacitively shunted junction (RCSJ) model [25]. The current through the junction in this model is

$$I = I_c \sin(\Delta\phi) + \frac{V}{R} + C\frac{\mathrm{d}V}{\mathrm{d}t} \,. \tag{2.15}$$

Here, the resistance describes the dissipation over a junction at finite voltage while capacitance is the shunting capacitance between electrodes of the junction. Substituting the AC Josephson relation from Eq. (2.11) and using the dimensionless variable $\tau \equiv \sqrt{2eI_c/(\hbar C)}t$, Eq. (2.15) leads to an equation describing the dynamics of the phase variable

$$\frac{\mathrm{d}^2(\Delta\phi)}{\mathrm{d}\tau^2} + \frac{1}{Q}\frac{\mathrm{d}(\Delta\phi)}{\mathrm{d}\tau} + \sin(\Delta\phi) = \frac{I}{I_c} \,, \tag{2.16}$$

where $Q \equiv RC\sqrt{2eI_c/(\hbar C)}$ describes the quality factor of a junction. The junction is called underdamped if $Q > 1/2$ and overdamped if $Q < 1/2$.

2.6 Improvement of tunneling characteristics by vacuum thermal annealing

Tunnel junctions often have problems with stability at room air and temperature: Junctions tend to age. Aging is manifested as a gradual increase of the tunneling resistance R_T over time. Instability is a severe drawback when considering commercial and practical applications of tunnel junctions for nanoelectronics.

There are several possible mechanisms for aging, such as adsorption of moisture or other impurity molecules into the barrier. This effect can be reduced by storing junctions in vacuum [35] or by passivating the metal films by growing a protective layer on top [36]. In addition, significant mechanism for aging can be the relaxation of the crystal structure of the oxide barrier. Typically metal–insulator–metal junctions are fabricated with vacuum evaporation techniques as described in section 2.1, and therefore the metal substrate onto which oxide is grown does not initially form a perfect crystal structure, but is more likely polycrystalline or amorphous. The relaxation of a glassy structure can take months at room temperature. In addition, the chemisorbed oxygen molecules on the barrier surface may enchance the instability of the junction [36]. However, the relaxation of the barrier can be artifially accelerated by a thermal annealing process. During the annealing, film temperature is first increased by heating it up for some time and then allowed to cool down. The heating step creates a disorder to the film, and if the cool–down is performed too rapidly, the film could remain in disordered phase (quenching). However, with

slow enough cooling the process can be considered to be quasistatic, i.e. the system goes through the equilibrium points at each moment, resulting in the energetically favourable configuration.

The influence of thermal annealing to tunnel junction characteristics and its aging was studied with several Al–AlO_x–Al tunnel junction samples containing either a single junction or two junctions in series. Single junction samples were made for studies of influence of annealing to superconducting properties of Al–AlO_x–Al junctions, while two junction samples allowed to probe the changes in charging effects. All samples were sub–micron sized, having a nominal area of $\sim$0.05 or $\sim$0.15 μm^2 checked by a scanning electron microscope (SEM). Samples were post–oxidized before breaking the vacuum to avoid the adsorption of moisture into the barrier.

2.6.1 Annealing procedure and complete stabilization

The annealing setup consisted of a vacuum chamber, connected to a diffusion pump station equipped with a liquid nitrogen trap to avoid contamination of the chamber with oil fumes. The base pressure of the system was $< 10^{-3}$ mbar during the whole annealing process. The heating element was a cylindrically shaped Boralectric® tubular heater HT–91 [37], containing a graphite filament covered with boron nitride. The maximum achievable temperature in this setup is 1200 °C, limited by the heating element. Cylidrical geometry was chosen for the heater because it provides a spatially uniform temperature profile on the sample stage. In addition, the vacuum chamber included a loading chamber with a sample stage attached to a slideable rod, allowing us to slide samples into the heating element. The sample stage had a copper block, where the sample and K–type thermocouple were attached to monitor and record temperature during annealing runs. Temperature as a function of time during a typical annealing cycle of 400 °C is presented in Fig. 2.3.

Figure 2.4 shows the aging of non–annealed samples and results for annealing at temperatures 200 °C, 300 °C and 400 °C. The effect of organic impurities on aging can be observed by comparing non–annealed samples. Substrates whose surface was plasma cleaned after developing (Fig. 2.4, dashed line) by exposing them to O_2 plasma in a RIE chamber showed remarkable reduction of aging compared to samples where cleaning was not performed before metal deposition (Fig. 2.4, solid line). For all annealed samples, the cleaning process was performed. The cleaning process should remove the residues of organic molecules, but it needs to be gentle enough to minimize the etching of areas of non–developed resist. More interestingly, annealing samples thermally at temperatures of 350 °C–450 °C showed complete stabilization. Some of these samples were checked a year after the fabrication and no change in the

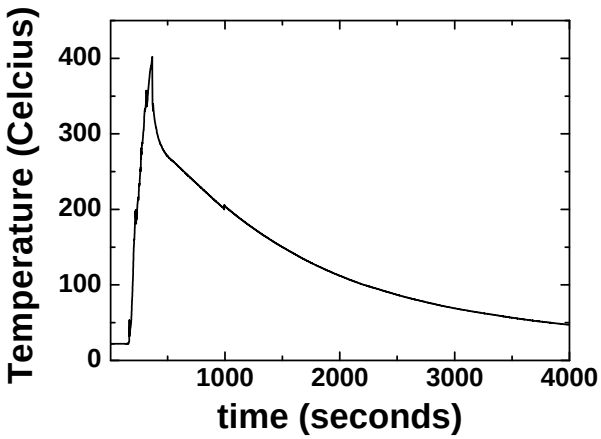

FIGURE 2.3 Temperature profile of the sample stage during 400 °C annealing cycle.

resistance was observed. However, temperatures below 350 °C are not high enough to stabilize the junctions and temperatures of 500 °C and above destroyed samples, typically leading to an open circuit situation. Annealing of samples leads to a significant increase in tunneling resistance (reduction of conductance), which varied from a factor of 2 to a maximum of 8 typically ranging between factors 2 and 4. The range of initial R_T varied from 1 kΩ to 200 kΩ. However, no clear correlation between the amount of increase and initial resistance was found.

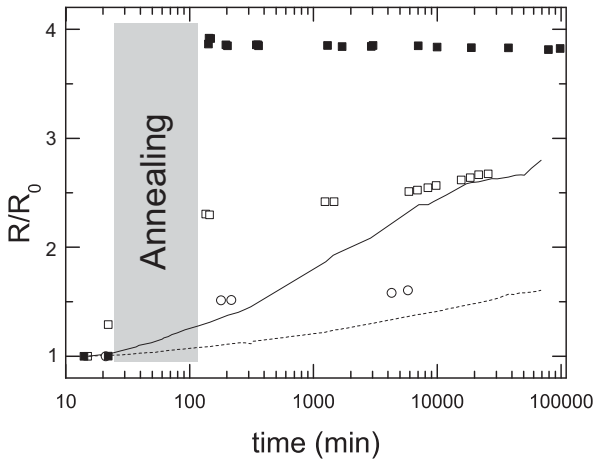

FIGURE 2.4 Tunneling resistance vs. time. Non–annealed samples with and without plasma cleaning of the substrate before metal deposition are presented with dashed and solid lines, respectively. Open circles represent aging with annealing temperature of 200 °C, open squares 300 °C and filled squares 400 °C. Gray box represents time of annealing. All resistances are normalized with initial resistance R_0 at time zero.

2.6.2 Low temperature characterization of samples

Normal state tunneling properties for samples containing two junctions were measured before and after annealing at 400 °C. Tunneling conductance $\mathrm{d}I/\mathrm{d}V$ was determined as a function of bias voltage by a standard lock–in technique, where a low frequency (17 Hz) AC excitation signal was added to a DC voltage bias and the current response of the sample was measured. All normal state measurements were carried out in a helium transport dewar, where the sample was attached to a dipstick sample stage by varnish and electrical contacts made by wirebonding. The low bias voltage ($|V| < 20$ mV) part of the tunneling conductance spectrum provides information on the charging energy of the system, from which the capacitance of the junctions can be estimated (see Fig. 2.5 (a)). The charging energy can be obtained from the depth of the weak Coulomb blockade dip as indicated by Eq. (2.6). Typical charging energies ranged from 9.8 μeV to 53 μeV, correponding to capacitances between 8.2 fF and 1.5 fF. Usually, charging energy increased by 5%–10% in annealing treament. However, two samples showed a reduction of charging energy by $\sim$18%.

The conductance spectrum at high bias voltages (Fig. 2.5(b)) deviated from the parabolic voltage dependence expected from Eq. (2.3) and showed several resonance peaks before annealing. After annealing, the spectrum was observed to have a parabolic shape and the resonances disappeared. Usually resonances in the tunneling spectrum are caused by unwanted impurities within the barrier, allowing resonant or inelastic tunneling at specific energies [19]. In addition, the deviation of the shape from that predicted by the elastic tunneling model supports this finding. Change in the tunneling behavior indicates the healing of the barrier due to the annealing process. Also the strenght of the voltage dependence of the tunneling conductance has been reduced, i.e. the curvature parameter V_0 in Eq. (2.3) has been increased by the annealing. The increase in V_0 together with increase of the charging energy and tunneling resistance indicates the increase in the height ϕ_0 and the effective thickness d of the barrier. The reduction of the capacitance (increasing charging energy) however, is not enough to conclude that the effective thickness has increased, since capacitance depends also on the dielectric constant of the barrier. The change in the absolute values is difficult to estimate due to deviation of the tunneling spectrum from V^2 dependence before annealing. However, a fit to the post–annealed spectrum provides $d = 9.4$ Å and $\phi_0 = 1.6$ eV for the sample in Fig. 2.5. All samples here were fabricated in a high vacuum evaporator with base pressure of 10^{-6} mbar. Samples fabricated in UHV conditions (base pressure 10^{-9} mbar) after plasma cleaning of the substrate typically have a weaker initial aging and they always show a quadratic conductance spectrum without resonances. This

result indicates that the initial evaporation conditions also have a significant effect on the junction quality. However, very recent annealing experiments for UHV samples show increased tunneling resistance and stabilization.

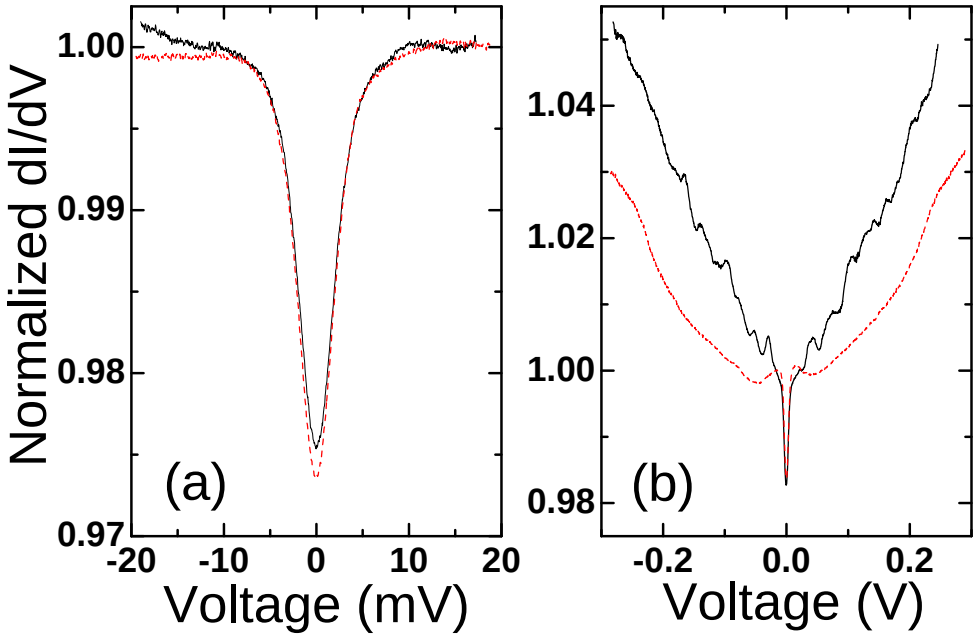

FIGURE 2.5 Tunneling conductance $\mathrm{d}I/\mathrm{d}V$ vs. bias voltage spectrum in units of G_T before (solid, black) and after annealing (dashed, red) measured at 4.2 K. (a) A narrow spectrum with the signature of a weak Coulomb blockade. (b) Wide bias voltage range tunneling spectrum.

In addition to the improved junction quality, an improvement of Al film quality was observed in treatments. Quality of films was checked by measuring the resistivity of a 70 nm thick and 550 nm wide Al wire at 4.2 K before and after thermal treatment at 400 °C. The film resistivity decreased by ∼30% from 5.1 to 3.4 μΩcm, corresponding to an increase in mean free path from 7.7 to 12 nm. However, high resolution SEM images shown in Fig. 2.6 showed no difference in the film grain structure.

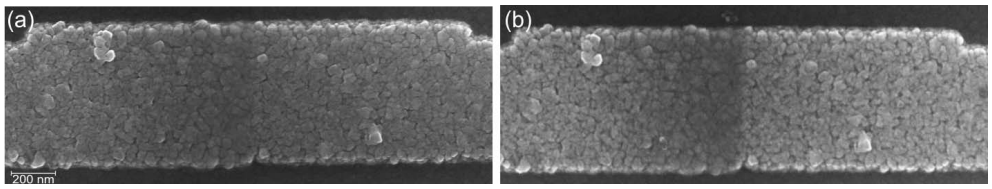

FIGURE 2.6 High resolution SEM image of an Al wire before (a) and after (b) annealing at 400 °C.

Superconducting properties of single junction samples were determined before and after annealing. All experiments were perfomed in a plastic dilution refrigerator with a base temperature of 50 mK [38]. Typical I–V characteristics before and after annealing are presented in Fig. 2.7(a), showing a clear superconducting gap and supercurrent at zero voltage bias. The inset shows a zoom–in to the sub-gap regime. Reduction of the current and slope in the quasiparticle branch $eV > 2\Delta$ corresponding to an increase in tunneling resistance is clearly observable. The size of the superconducting gap Δ showed no significant change upon annealing, as verified with the tunneling conductance spectrum shown in Fig. 2.7(b). In addition, the supercurrent peak is reduced as expected from the relation (2.14), once Δ is fixed. However, Eq. (2.14) holds exactly only for fluctuation–free critical current. Curiously, there exist several resonances in the sub–gap current, close to the supercurrent (Fig. 2.7(a)). Resonances are typically be caused by the coupling of the junction to its electromagnetic environment [39], and they seem to be smeared out after annealing.

To study the supercurrent branch $V \sim 0$ more carefully, switching currents were measured by a cumulative histogram method (a good description can be found e.g. in [40]). In this method, a set of current pulses (total amount of 10000) of constant height I_p was injected into the sample and the number of switching events was measured by counting the number of voltage responses to the current pulses. The frequency of the pulses was 100 Hz and duty cycle 5%, corresponding to a pulse duration of 500 µs. In addition, the sample was shunted by ∼10 kΩ to reduce the electrical RC time constant of the circuit. Without the shunt resistor, the sample is not able to recover from a switching event before the next pulse, because the time constant related to junction resistance (∼10 MΩ) and line capacitances can easily be of the order of 0.1 s. Cumulative histogram method automatically provides the switching probability as a function of current (pulse height). Results for the same sample as in Fig. 2.7(a) and (b) are shown in Fig. 2.7(c). The switching current, defined as the value where probability is 0.5, is reduced to one fifth of the original value due to thermal treatment.

The fluctuation–free critical current of the sample can be estimated from the Ambegaokar–Baratoff relation (2.14) and the capacitance of a single junction can be estimated from experiments for two junction samples of the same area. These parameters give estimates of Josephson coupling energy (2.13) and charging energy (2.4), providing the ratio $E_J/E_C \sim 1.8$. Therefore, the samples are in the underdamped regime, where the prediction for the dependence of the switching current (including fluctuations) on the tunneling resistance is $I_{\mathrm{SW}} \propto R_T^{-3/2}$ [41] for the unshunted junctions. Hence, the reduction of the switching current to one fifth is fully

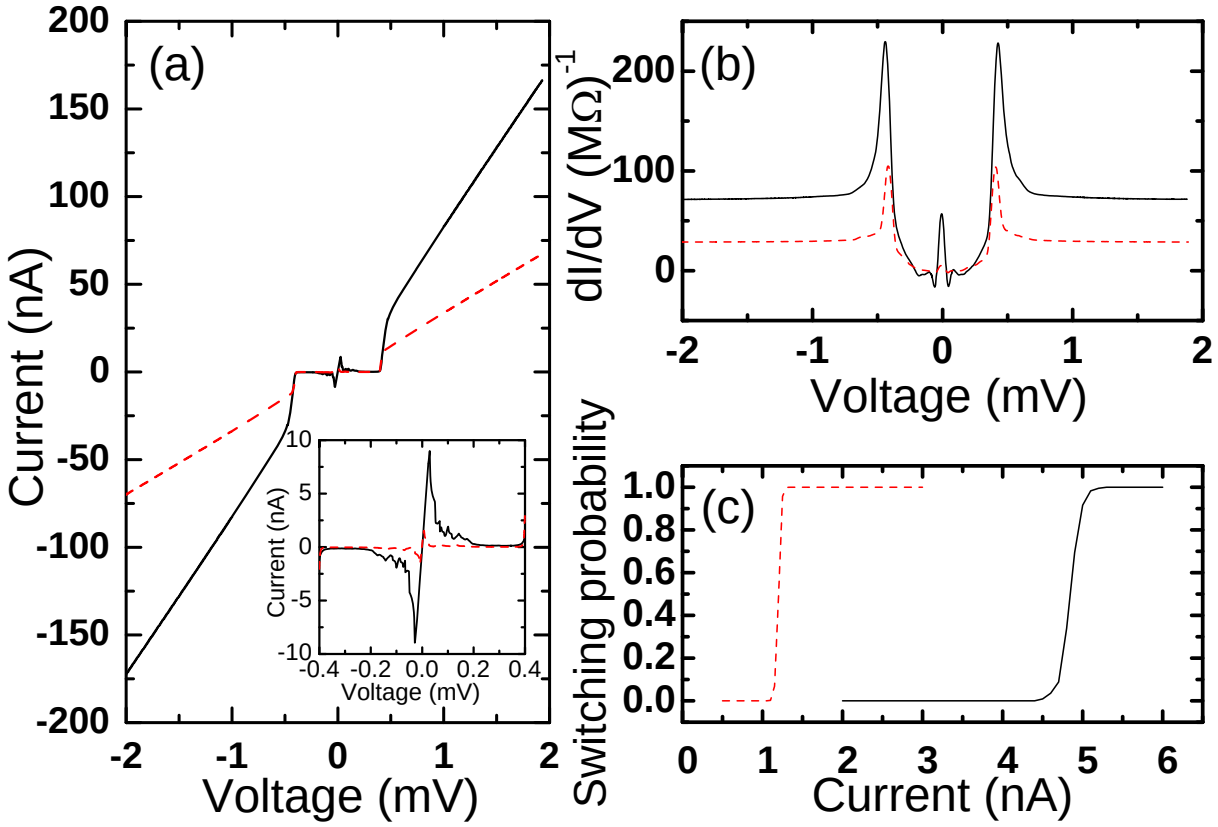

FIGURE 2.7 (a) Typical I–V curve and (b) differential conductance for single Josephson junction sample before (black, solid) and after (red, dashed) annealing at 400 °C. Inset in (a) is the zoom–in to the sub–gap current. (c) Measured switching probability of a sample before and after annealing.

consistent with the increase in R_T by a factor of three (Fig. 2.7).

In addition to bare Al–AlO_x–Al junctions also several Al–AlO_x–Cu junctions were annealed. This kind of junction is typically used in NIS thermometry and cooling with Cu as normal metal. Thermal annealing might improve the subgap properties of the junctions, leading to improvement of their use e.g. in thermometry. One source of subgap current is finite life–time effects discussed above in context of NIS tunneling. Life–time broadening may be related to the film quality and therefore the thermal annealing of Al should reduce the broadening parameter. However, all samples containing copper resulted in an open circuit condition already at temperatures of 200 °C. SEM images taken after annealing revealed an obvious reason for this behavior: the Cu film was observed to be partly ripped off or degraded badly, see Fig. 2.8. The most probable explanation for degradation is that Cu has a weak adhesion to SiO_x and SiN surfaces, therefore even relatively low temperatures are enough to "lift–off" the film from the substrate. Usage of a very thin (few nanometer

thick) film of titanium as an adhesion layer and deposit Cu on top might alleviate the problem.

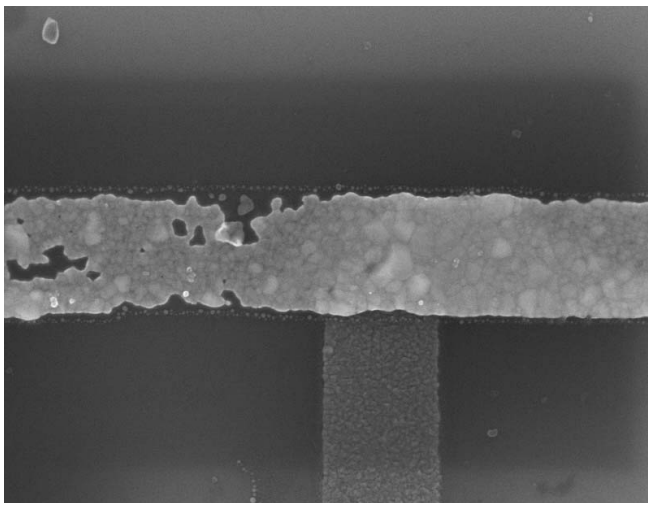

FIGURE 2.8 SEM image of Al–Al_x–Cu junction after annealing treatment.

Chapter 3

Thermometry and cooling with NIS junctions

The principles of normal metal–insulator–superconductor (NIS) junctions in thermometry and cooling are introduced in this chapter. In addition, a discussion about the effects of charging energy on thermometry is included. Results of this chapter are used for studies of thermal transport and cooling in low–dimensional nanostructures presented in the next chapter.

3.1 NIS thermometry

Non–linear current–voltage (I–V) characteristics of NIS junctions, obtained from Eq. (2.8) can be used for sensitive thermometry and have been widely used in several sub–kelvin thermal transport experiments [42, 43, 28, 44, 4, IV]. The original experimental realization of the concept was first perfomed by Rowell and Tsui already in 1976 [45].

The tunneling current equation (2.8) for an NIS junction can be written in a symmetric form

$$I(V,T) = \frac{1}{2eR_T}\int_{-\infty}^{\infty} n_S(E)\,[f_N(E-eV) - f_N(E+eV)]\,\mathrm{d}E \tag{3.1}$$

In this form, the Fermi–Dirac distribution of the superconductor has been eliminated, showing that current through an NIS junction is a function of only electron temperature and therefore independent of the temperature of the superconductor. However, the DOS term $n_S(E)$ implicitly includes the superconductor temperature since it is a function of superconducting gap. Therefore, equation (3.1) above can be considered to be independent of the superconductor temperature when the condi-

tion $T < 0.5T_C$ (T_C being critical temperature of the superconductor) holds.

Thermometry is usually carried out by current biasing the thermometer at a constant current and measuring the voltage response. These voltage–to–temperature (V–T) calibration curves are ideally determined by only two parameters: superconducting gap Δ and tunneling resistance R_T, both of which can be determined accurately from I–V characteristics of the junction. This property makes the NIS junction in principle a primary thermometer. However, there are deviations from this ideal behavior caused by e.g. excess noise heating of the electron gas [46], finite sub–gap current [32, 27] and charging effects [II].

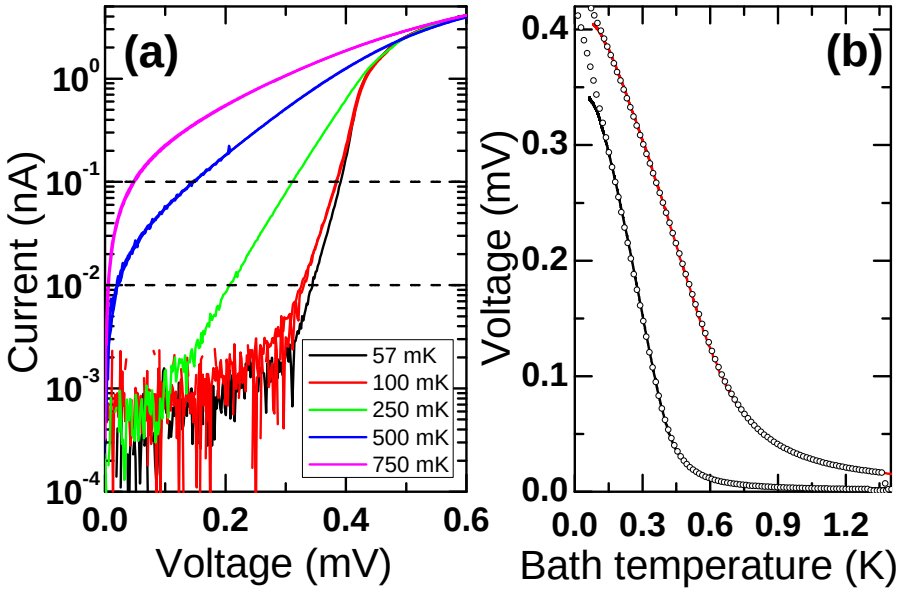

FIGURE 3.1 (a) Typical measured sub–gap current–voltage characteristics of a SINIS thermometer ($R_T = 50\,\mathrm{k\Omega}$) at different temperatures. Dashed horizontal lines from top to bottom correspond to current biases of 100 pA and 10 pA, respectively. (b) Voltage of a SINIS thermometer vs. bath temperature at current biases presented in (a), black line corresponds to 10 pA and red line to 100 pA value. Open circles represent values calculated with Eq. (3.1).

The voltage signal of a thermometer, and therefore its responsivity $|\mathrm{d}V/\mathrm{d}T|$ can be enhanced by using a structure containing two junctions in series (SINIS) instead of one (NIS). Measured I–V characteristics at different bath temperatures of a typical SINIS thermometer are shown in Fig. 3.1 (a). It can be immediately observed that different current bias values give different responsivities for different temperature ranges. Two horizontal lines correspond to two different current bias points of 10 pA and 100 pA, respectively. Low bias value shows a gain in sensitivity at low temperatures ($T < 400$ mK), while at high temperature ($T > 400$ mK) sensitivity is lost. The high current bias value provides more sensitivity at high temperature,

but sensitivity is reduced at low temperatures. The best results in thermometry are obtained by repeating experiments with different bias points for different temperature ranges. However, too high bias current can cause significant self–heating of the thermometer at the lowest temperatures due to power dissipation in the normal metal. The practical limit for high bias depends on the resistivity of the normal metal. However, the current should not exceed the limit where the corresponding voltage response V is larger than the superconducting gap, i.e. $V_{\mathrm{SINIS}} > 2\Delta/e$. After this, the junction itself induces significant heating [12]. The self–heating effects in thermometry are especially important in structures where the heat flow to the surroundings of the normal metal is strongly limited, such as samples with small normal metal islands or suspended nanostructures.

In addition to self–heating of the thermometers, self–cooling effects can be significant, if the tunnel junction is improperly biased, i.e. if voltage yields $V_{\mathrm{SINIS}} \sim 2\Delta/e$. Fortunately, junctions for thermometry are typically small, having relatively large tunneling resistances and thus self cooling effects are negligible. A detailed discussion about cooling with SINIS structures is in section 3.3.

A typical voltage–to–temperature response of a SINIS thermometer is shown in Fig. 3.1(b). Solid lines correpond to two different current bias values presented in Fig. 3.1(a), 10 pA (black) and 100 pA (red). Open circles are numerical calculations according to Eq. (3.1) for corresponding current biases. Measured data shows a deviation from theoretical calculations at temperatures below ∼150 mK. This is most likely due to noise heating of the electron gas, i.e. due to coupling of electrons to the electromagnetic environment [46]. Therefore at the very lowest temperatures electron temperature deviates from the bath (phonon) temperature. Typically noise power in experiments is of the order of 5–10 fW, depending on the filtering in the cryostat and the electrical impedance of the junctions.

The finite life–time broadening of the DOS, discussed in the chapter 2 has effects on the voltage–to–temperature response of a SINIS thermometer. Calculated I–V curves with different values of the broadening parameter Γ are shown in Fig. 3.2(a), and corresponding V–T curves in Fig. 3.2(b) with current bias shown by dashed line in (a). All numbers are presented in scaled units and the bias point corresponds to 10 pA current for a junction with $R_T = 20$ kΩ and $\Delta = 220$ μeV. These are typical values for thermometer junctions with Al as the superconductor. The finite life–time broadening affects the response curves in similar way as noise heating. However, these two effects can be distinguished from each other by looking at the sub–gap current voltage characteristics. Temperature changes the exponential slope at the gap edge, while finite Γ changes the current in the sub–gap regime. Typical values in measured Al films $\Gamma/\Delta \sim 2 \cdot 10^{-4}$ yield no noticeable effect in thermometer

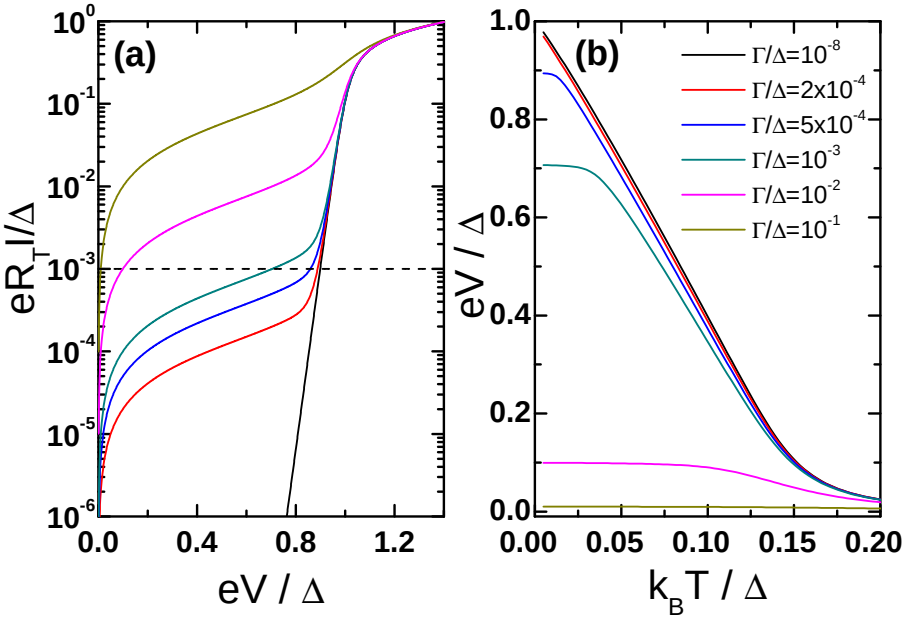

FIGURE 3.2 (a) Current–voltage characteristics calculated at temperature of 50 mK with different values of the DOS broadening parameter Γ, values and corresponding colours are shown in (b). (b) SINIS thermometer voltage–to–temperature response with current bias corresponding horizontal dashed line in (a).

response, while e.g. with values reported for Nb tunnel junctions $\Gamma/\Delta \sim 10^{-2}$ [30] the response of the thermometer is reduced drastically. Therefore, practical implementation of SINIS thermometers based on evaporated Nb films can be difficult or even impossible.

In summary, the main advantages of SINIS thermometry are small size, low self–heating, good responsivity at sub–kelvin temperatures, simple operation with DC–voltages, ease of integration into the thermal system under study and existing high–frequency read–out schemes [47]. In addition, SINIS structures are convenient for use as a local probe for temperature in nanoscructures. However, SINIS structures are not suitable for thermometry in magnetic fields, since the sensitivity of the thermometer is reduced due to suppression of the superconducting gap by an external magnetic field.

3.2 Influence of charging effects on thermometry

SINIS structures containing small junctions (small capacitance) connected to small islands (small self–capacitance) may have significant charging energy compared to the temperature scales which are measured with them. In other words, the condition $E_C \gg k_B T$ can be satified easily in sub–micron sized SINIS structures at sub–Kelvin

temperatures, as demonstrated recently with a heat transistor [48] and hybrid single electron pump [49]. In addition, charging effects (Coulomb blockade) will have consequences on thermometry with SINIS structures.

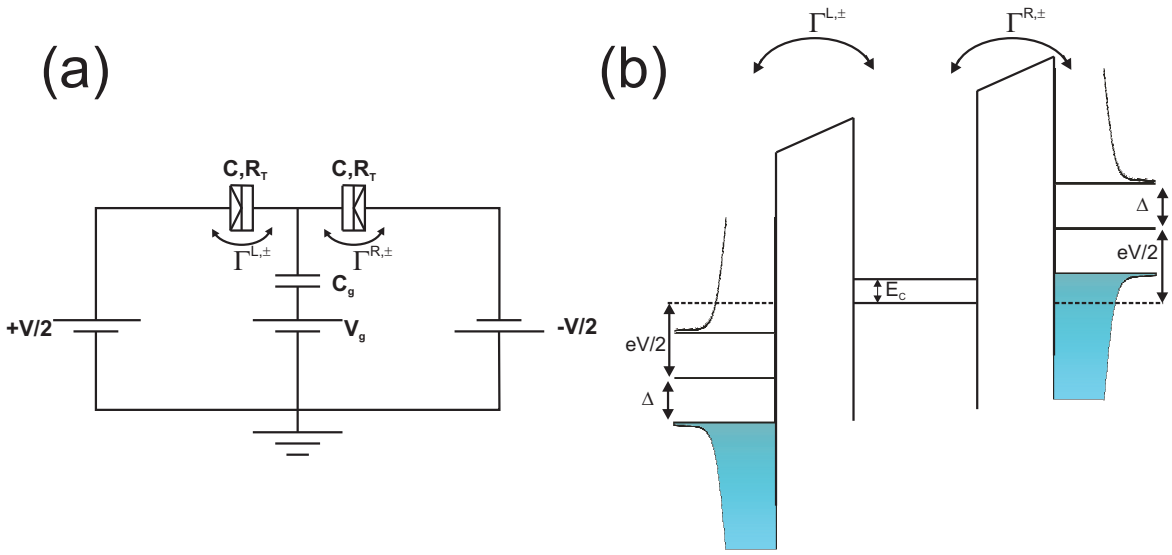

FIGURE 3.3 Schematics of (a) circuit and (b) energy level diagram of SINIS thermometer with gate.

Let us consider a system of two NIS junctions connected in series having identical capacitances C and resistances R_T with an additional gate electrode having a gate capacitance C_G located in close proximity to the normal metal island. A schematic of the circuit and energy level diagram of the system are shown in Fig. 3.3, and they are similar to the hybrid single electron transistor setup described in publications [49,50]. The I–V characteristics of the junction are modified by the charging energy, and can be modulated with an external gate voltage V_G. The tunneling rates onto (+) and off (-) the island through left L and right R junction can be written according to Ref. [50] in the form

$$\Gamma^{i,+} = \frac{1}{e^2 R_T} \int_{-\infty}^{\infty} n_S(E) f_S(E) \left[1 - f_N(E - E_n^{i,+})\right] \mathrm{d}E \tag{3.2}$$

$$\Gamma^{i,-} = \frac{1}{e^2 R_T} \int_{-\infty}^{\infty} n_S(E) f_N(E - E_n^{i,-}) \left[1 - f_S(E)\right] \mathrm{d}E \,, \tag{3.3}$$

where $i = \{L, R\}$ and $E_n^{i,\pm} = \pm 2E_C(n + n_G \pm 0.5) \pm eV_i$ is the change in the electrostatic energy of the system when an electron tunnels onto (+) and off (-) the island, V_i being the bias voltage of the left or right junction. Here n is the number of excess electrons on the island ($n \in \mathbb{Z}$), $en_G = Q_G = C_G V_G$ additional gate charge and $E_C \equiv e^2/C_\Sigma$ is the charging energy with total capacitance of the island $C_\Sigma = 2C + C_G$. The gate

charge en_G is a continous variable and can be varied with gate voltage V_G. With $n_G = 0$, the Coulomb blockade is maximum while with $n_G = 0.5$ it is minimum. These are called closed and open gate situations, respectively.

The current through a SINIS structure can be calculated by solving the Master equation with detailed balance condition (see e.g. [51])

$$\Gamma^+(n)P(n) = \Gamma^-(n+1)P(n+1)\,, \tag{3.4}$$

where $\Gamma^\pm \equiv \Gamma^{L,\pm} + \Gamma^{R,\pm}$ and $P(n)$ is the occupation probability of charge state n on the island and obeys the normalization condition $\sum_{n=-\infty}^{\infty} P(n) = 1$. Furthermore, current through the SINIS is obtained from

$$I_i = -e\sum_{n=-\infty}^{\infty} P(n)\left[\Gamma^{+,i} - \Gamma^{-,i}\right]\,, I = I_L = -I_R\,. \tag{3.5}$$

In general, in the strong Coulomb blockade limit $E_C \geq k_BT$, the current needs to be solved by using numerical methods. However, with weak Coulomb blockade $E_C \ll k_BT$ the current can be written in an analytic form. At that limit and $n_G = 0$, the current next to the leading order with respect to $E_C/(k_BT)$ is (see appendix A)

$$I = I_{E_C=0} - \frac{E_C}{4k_BT_N}\frac{1}{R_T}\int_{-\infty}^{\infty} n_S(E)f_S(E)\left[\frac{1}{\cosh^2\left(\frac{E+eV/2}{2k_BT_N}\right)} - \frac{1}{\cosh^2\left(\frac{E-eV/2}{2k_BT_N}\right)}\right]\mathrm{d}E \tag{3.6}$$

Here, $I_{E_C=0}$ is the current with no charging effects, presented in Eq. (3.1) and T_N is the electron temperature in the normal metal. Figure 3.4 shows plots of the sub–gap current in the weak Coulomb blockade limit and current without charging effects present. At the weak Coulomb blockade regime, current through the junction is suppressed by an amount that depends on the ratio $E_C/(k_BT)$. With $E_C = 0.4k_BT$, the change in the voltage due to charging effects of the thermometer is $\lesssim$1% for low bias currents, corresponding to $\lesssim$5 mK correction in typical voltage to temperature calibration at low temperatures. Interestingly, $f_S(E)$ and thus the superconductor temperature cannot be eliminated from either form of tunneling current with E_C involved in Eqs. (3.2) and (3.6). However, the effect of the superconductor temperature is negligible for typical temperature differences achieved e.g. in coolers (200 mK) and it is typically only visible deep in the sub–gap.

I–V characteristics in the strong Coulomb blockade limit are calculated in Fig. 3.5 with three different values of charging energy. All calculations are performed for the closed gate (maximal Coulomb blockade) situation $n_G = 0$, and with the broadening parameter value of $\Gamma/\Delta = 2\cdot10^{-4}$. Temperature for the calculations is

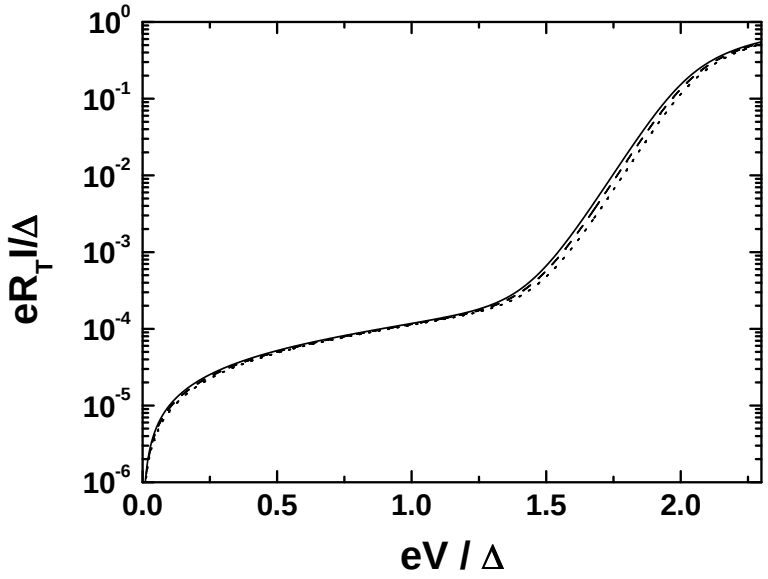

FIGURE 3.4 Sub–gap current current–voltage characteristics of a SINIS thermometer in the weak Coulomb blockade limit. Solid line is the calculation without charging energy, dashed line with $E_C/(k_BT) = 0.2$ and dotted line $E_C/(k_BT) = 0.4$, calculations are performed with $k_BT/\Delta = 0.02$ and $\Gamma/\Delta = 2 \cdot 10^{-4}$.

fixed $k_BT/\Delta = 0.02$ and $E_C/\Delta = 0$, 0.1 and 0.2. With typical Al values $\Delta = 220$ μeV these correspond to a temperature of 50 mK and charging energy of 0, 250 mK and 500 mK, respectively. Two dashed horizontal lines correspond to low and high current bias values of $eR_TI/\Delta = 2.3 \times 10^{-3}$ and $eR_TI/\Delta = 2.3 \times 10^{-2}$, correponding to 10 and 100 pA for a junction with $R_T = 50$ kΩ, respectively. Charging energy effectively shifts the I–V curves to higher voltages leading to an effective increase of the superconducting gap from Δ to $\Delta + E_C$.

V–T curves and corresponding responsivities $|\mathrm{d}V/\mathrm{d}T|$ calculated with the current bias and charging energy values above are shown in Fig. 3.6. Charging energy increases the responsivity of the thermometer, but also the shape of the V–T response is modified. With charging energy, a bump appears in the responsivity curve at temperatures around $k_BT = 0.15\Delta$ for the low bias and $k_BT = 0.2\Delta$ at high bias. In addition, from responsivity curves it can be easily observed that two different bias points have different optimal temperature ranges: low bias responsivity is high at temperatures $k_BT < 0.15\Delta$ (380 mK for Al), but drops quickly to unpractically low values, while high bias responsivity stays useful up to much larger temperatures.

Effects of the gate voltage on response and responsivity are shown in Fig. 3.7. All calculations are performed with $E_C/\Delta = 0.2$. The gate charge changes

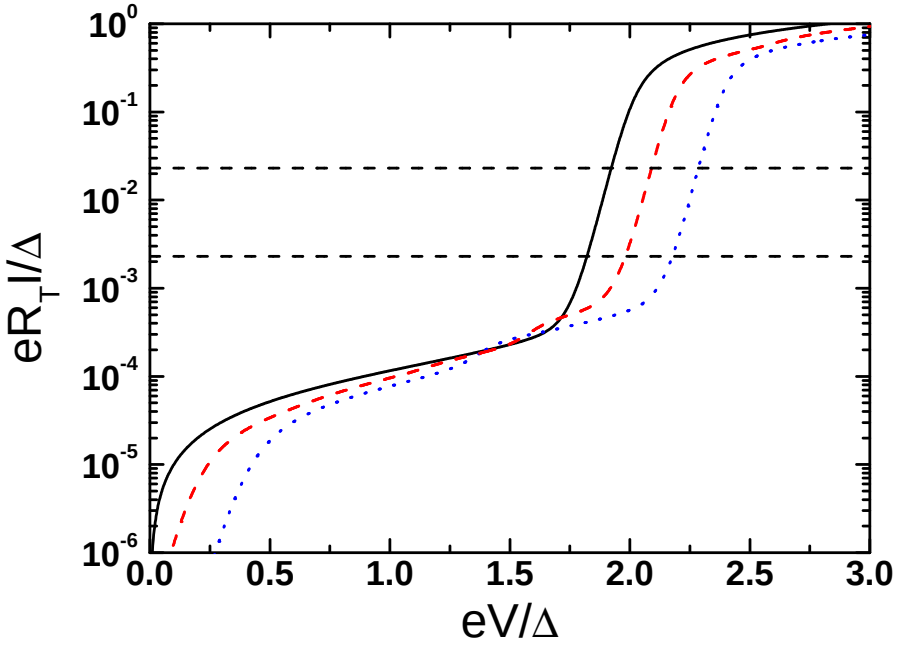

FIGURE 3.5 Sub–gap current–voltage characteristics calculated with three different values of $E_C/\Delta = 0$ (black, solid), 0.1 (red, dashed) and 0.2 (blue, dot) in closed gate situation $n_G = 0$, $k_BT/\Delta = 0.02$ and $\Gamma/\Delta = 2 \cdot 10^{-4}$. Two dashed horizontal lines correspond to the current bias values of $eR_TI/\Delta = 2.3 \times 10^{-3}$ and $eR_TI/\Delta = 2.3 \times 10^{-2}$.

the response of the thermometer. Open gate $n_G = 0.5$ configuration provides the same zero–temperature voltage as the calculation without charging energy, albeit the shape of the curve is still different from situation $E_C = 0$ as seen from the responsivity curve in Fig. 3.7 (b). Responsivity of the thermometer as a function of gate charge at different temperatures ranging from $k_BT/\Delta = 0.01$ to 0.18 is shown in Fig. 3.8. The low temperature results show sharp peaks for closed and open gate situations, while at intermediate regions responsivity is flat, independent of the gate charge. At higher temperatures, sharp peaks broaden into a sinusoidal gate dependence with decreasing amplitude as temperature in increased. Responsivity can be enhanced by 30 % at the lowest temperatures by closing the gate.

Charging effects should be taken into account in thermometry for SINIS thermometers that are small in size and connected to small islands. Such structures are typically used as a local probe to monitor e.g. bulk temperature of the sample. The measured Coulomb blockade of a typical solitary bulk thermometer with a junction area of $\sim$0.05 µm^2 is shown in Fig. 3.9. The corresponding charging energy of a sample is 200 mK according to Eq. (2.6), 200 mK corresponds to $E_C/\Delta = 0.08$ for Al with $\Delta = 220$ µeV. Therefore, to perform accurate and reliable thermometry at tem-

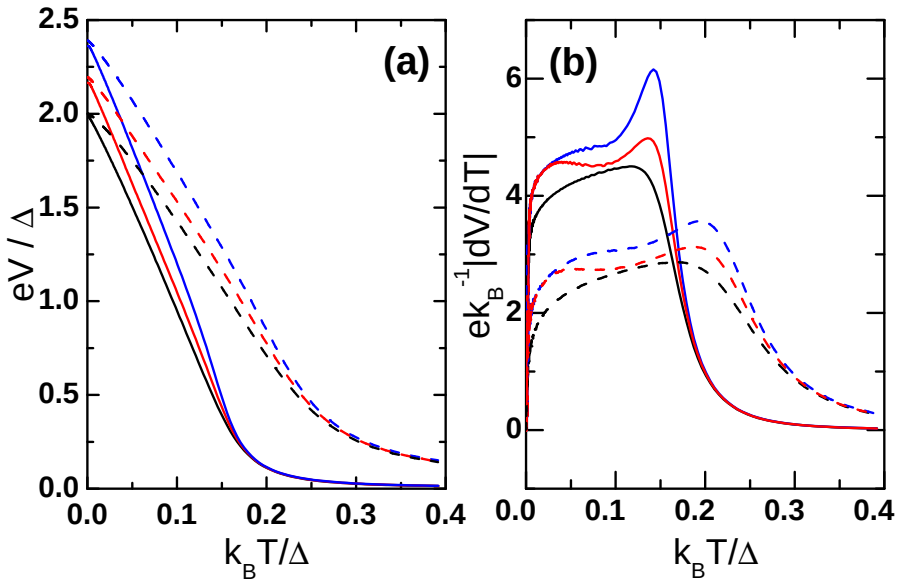

FIGURE 3.6 (a) Calculated voltage response vs. temperature curves of a SINIS with three different charging energies $E_C/\Delta = 0$ (black, bottom), 0.1 (red) and 0.2 (blue, top) with $n_G = 0$. Solid lines correspond to low bias current ($eR_TI/\Delta = 2.3 \times 10^{-3}$) and dashed lines high bias current ($eR_TI/\Delta = 2.3 \times 10^{-2}$) values, respectively. (b) Responsivity $|\mathrm{d}V/\mathrm{d}T|$ of a thermometer calculated from (a).

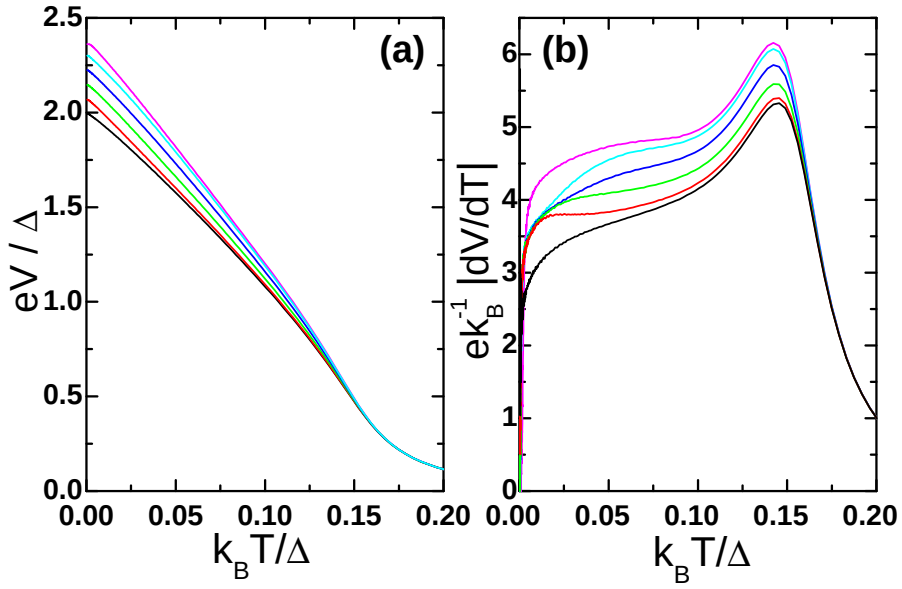

FIGURE 3.7 (a) Calculated SINIS voltage response vs. temperature curves for $E_C/\Delta = 0.2$ and current bias of $eR_TI/\Delta = 2.3 \times 10^{-3}$ with varying gate charge from an open gate $n_G = 0.5$ (bottom) to a closed gate $n_G = 0$ (top) with interval of 0.1. (b) Responsivity $|\mathrm{d}V/\mathrm{d}T|$ of a thermometer calculated from (a), top corresponding situation $n_G = 0$ and lowest $n_G = 0.5$.

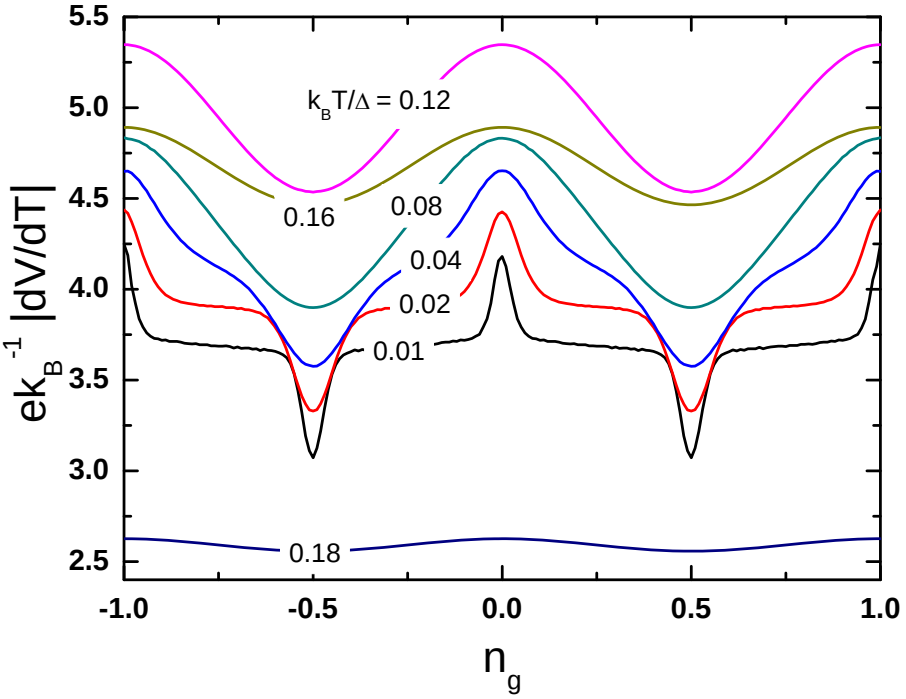

FIGURE 3.8 Responsivity of a SINIS thermometer as a function of gate charge with different scaled temperatures from $k_BT/\Delta = 0.01$ to 0.18. $E_C/\Delta = 0.2$ and current bias $eR_TI/\Delta = 2.3 \times 10^{-3}$ are used in the calculation.

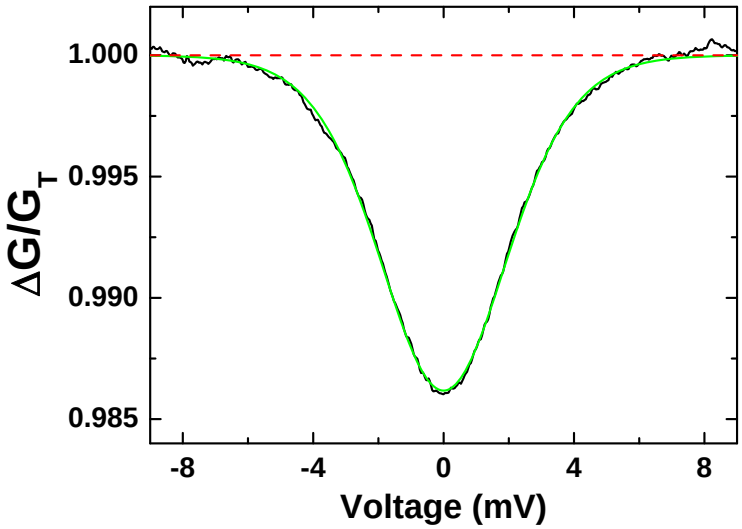

FIGURE 3.9 Measured Coulomb blockade of a solitary bulk SINIS thermometer at 4.2 K. Conductance is normalized with G_T (red, dashed line) and green solid line represents weak Coulomb blockade theory.

peratures below 200 mK the charging effects should not be completely neglected in analysis.

3.3 Cooling with NIS junctions

In addition to thermometry, NIS junctions can be used also for cooling the electron gas of the normal metal island. The basic principle of cooling by an NIS junction is based on the existence of the energy gap Δ in the superconductor. As seen from the tunneling current equation (2.8), an electron from the normal metal cannot enter the superconductor, unless it has at least energy Δ. At finite temperatures, electrons obey the Fermi–Dirac distribution of the normal metal, therefore there are hot electrons that can tunnel to the superconductor even at bias voltages $eV < \Delta$. Since only hot electrons escape, the temperature of remaining electrons on the normal metal island is lowered. This process is sometimes called evaporative cooling, and is analogous to that used in e.g. magneto–optic traps where hot atoms are evaporated from the atom cloud by changing the trapping potential [52]. A schematic view of the operation of a NIS cooler is presented in Fig. 3.10. The heat flow from the normal metal to the superconductor is [12]

$$\dot{Q}_{\mathrm{cool}} = \frac{1}{e^2 R_T} \int_{-\infty}^{\infty} (E - eV) n_S(E) \left[f_N(E - eV) - f_S(E) \right] \mathrm{d}E \, . \tag{3.7}$$

Unlike the electric current in Eq.(2.8), heat current cannot be written independently of $f_S(E)$, and therefore heat current depends both on temperature of the normal metal island and of the superconductor. Optimal cooling power is achieved, when the cooler is biased close to the edge of the superconducting gap $V \sim \Delta/e$. At higher bias voltages heat flow changes its sign and heating starts to dominate. The optimum cooling power at different temperatures is also dependent on the energy gap [12]. To maximize the cooling power, the temperature of the superconductor must be as low as possible, which can be ensured by removing the injected hot quasiparticles as effectively as possible. The quasiparticle diffusion out of the superconductor can be realized by adding quasiparticle traps in close proximity to the superconductor [17] and by making the superconductor thick enough to improve the diffusion away from the junction region. The heat flow, and hence the cooling power can be doubled if two NIS junctions are connected in series (SINIS cooler).

In the operation of practical coolers, back–flow of heat reduces the perfomance of the cooler. The backflow of heat is due to quasi–particle recombination in the superconductor and back tunneling [53]. The cooler can be modelled in equilibrium with a power balance equation, where heat flow from the surroudings is equal to the heat flow from the normal metal island

$$P_{\mathrm{heat}} - P_{\mathrm{cool}} = 0 \, , \tag{3.8}$$

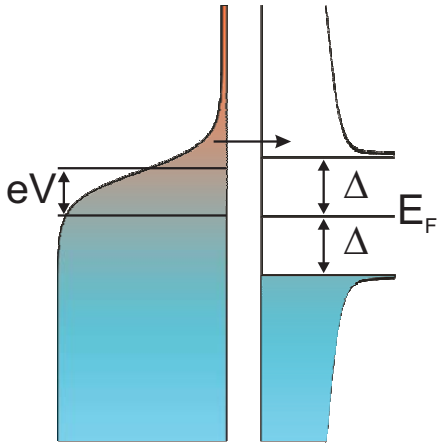

FIGURE 3.10 Schematics of the operation principle of NIS cooler.

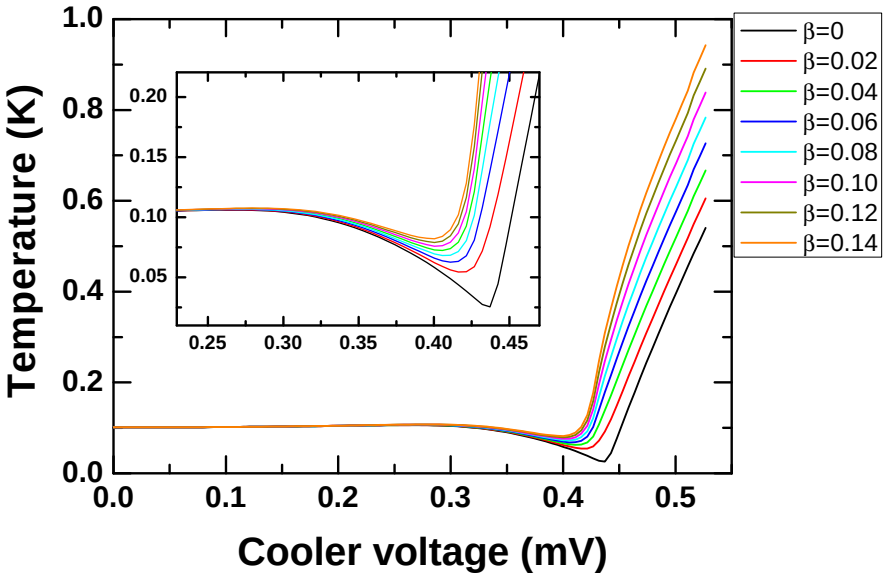

FIGURE 3.11 Calculated temperature vs. voltage curves with different values of back-flow parameter β.

where P_{cool} is the cooling power according to Eq.(3.7) and P_{heat} is the heat flow from the surroundings, which in general form is [53,54]

$$P_{\mathrm{heat}} = -A(T_e^n - T_{\mathrm{bath}}^n) + \beta(P_{\mathrm{cool}} + IV)\ . \tag{3.9}$$

The first term describes the thermal coupling of normal metal electrons with tem-

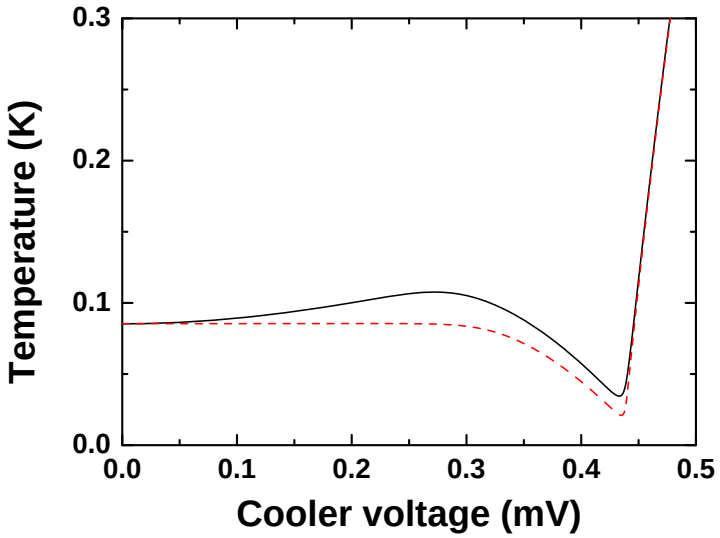

FIGURE 3.12 Black, solid line represents the calculated SINIS cooler temperature vs. voltage characteristics with the life–time broadened DOS $\Gamma/\Delta = 2.5 \cdot 10^{-4}$ and red, dashed line is the calculation without broadening.

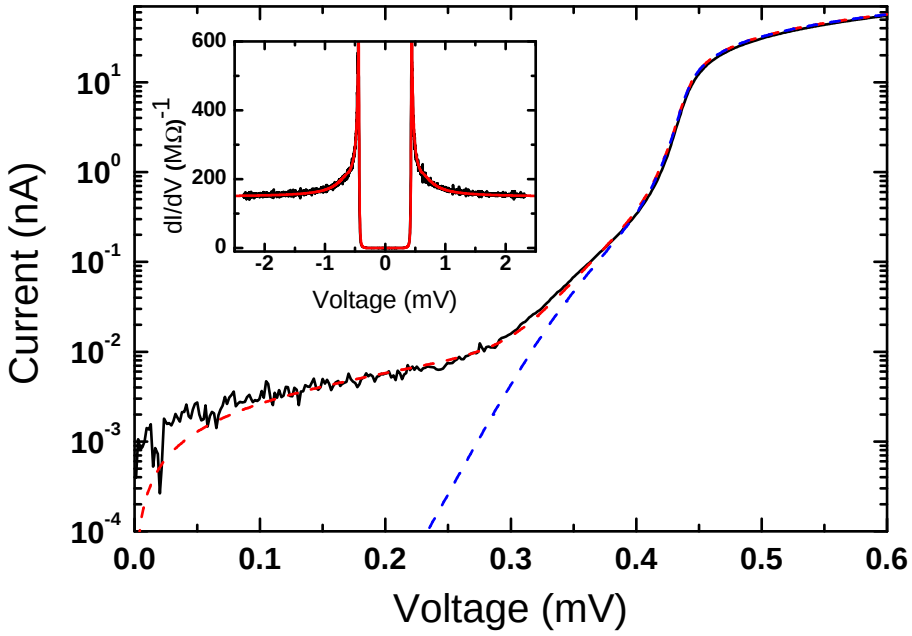

FIGURE 3.13 Black, solid line represents the measured SINIS cooler I–V characteristics, red dashed and blue dashed lines are the calculation with ($\Gamma/\Delta = 2 \cdot 10^{-4}$) and without finite life–time broadening, respectively. In both calculations, the self–cooling of a junction is taken into account. Inset shows differential conductance for measured data (black) and simulation (red). The parameters for the calculated curves are $R_T = 3.3$ kΩ and $\Delta = 220$ μeV.

perature T_e to the environment at temperature T_{bath}, A being the coupling strength. In the case of a cooler connected to a typical bulk material, the first term is described by electron–phonon coupling, with $A = \Sigma\Omega$, Σ is the coupling constant and Ω is the volume of the electron gas and $n = 4$–6 ($n = 3$ for one–dimensional case) depending on scattering mechanisms [55]. In the case of phonon mediated thermal conductance, A is independent of electron gas volume and $n = 2$–6 depending on the phonon mode and dimensionality [2, 56, 57, 58]. The second term in (3.9) is the back–flow of the heat from the superconductor due to recombination of quasiparticles and back–tunneling, where parameter $0 \leq \beta \leq 1$ decribes the fraction of the back–flowing heat absorbed by the normal metal. I is the current through, and V the voltage across the junction, hence IV describes the Joule power dissipated due to quasiparticles tunneling onto superconductor and backtunneling to normal metal. Electron temperature of the normal metal can be determined for each bias voltage of the cooler by solving the power balance equation (3.8) numerically. Calculated temperature vs. bias voltage curves with different values of back–flow parameter β are shown in Fig. 3.11. The model decribed above has been used in the next chapter to analyze coolers connected to a suspended nanowire. In addition, the life–time broadening of the DOS of the superconductor has an effect on cooling leading to heating in the sub–gap region, manifested as a small bump in the cooler voltage vs. temperature curves in the sub–gap region (Fig. 3.12). Modelling the cooler I–V characteristics, the life–time broadening must be taken into account, as demonstrated in Fig. 3.13.

The first experimental implementation of NIS cooling was demonstrated by the group of Martinis (Nahum et al. [59]) at NIST Boulder in 1994. Improvements of the cooler were made by the group of Pekola (Leivo et al. [42]) in Jyväskylä in 1996, where electron temperature of a normal metal island was reduced from 300 mK down to 100 mK. The group at NIST Boulder has even demonstrated the cooling of a "bulk" piece of material with SINIS coolers [43]. SINIS coolers are beneficial for cooling down small payloads for space applications, such as radiation detectors [60]. Results and discussion on cooling of low dimensional nanostructures with SINIS structures is discussed in more details in the next chapter.

Chapter 4

Thermal properties of suspended nanostructures

4.1 Fabrication of suspended structures

All suspended structures (membranes and bridges) in this thesis were fabricated from LPCVD grown low–stress SiN ordered from UC Berkeley Microfabrication Laboratory [61]. We first descibe the fabrication process of photo–masks for membranes and then wet and dry etching techniques to make membranes and structural release of suspended beams. Thin SiN membranes were directly used as suspended samples in strain sensing (chapter 5), and they were used as templates for suspended beams described in this chapter.

Since photo–lithography with ultraviolet (UV) light is the easiest and quickest way to obtain structures with dimensions of several microns, fabrication of SiN membranes begins with the fabrication of a photo–mask. Typical membrane dimensions in our experiments ranged from 50 µm $\times$ 50 µm to 300 µm $\times$ 300 µm. The template for a photo–mask was a microscope glass plate coated with 100 nm of chromium (Cr) by vacuum evaporation in a Balzers high–vacuum evaporator. After evaporation, a single layer of 4% PMMA in anisole solvent was spun on Cr and baked for three minutes. Structures, squares in the case of membranes, were patterned on PMMA with EBL and developed with 1:3 MIBK:IPA solution. The developing step was followed by wet etching of Cr from the exposed areas by immersing the sample in a mixture of 30% potassium ferrocyanide ($K_3Fe(CN)_6$) and 50% sodium hydroxide (NaOH) with concentration of 1:3 for about one minute and then rinsed with distilled water. The etching step made the exposed areas transparent to UV light.

The template for membranes was a (100) Si chip, both sides coated with LPCVD

grown SiN with typical thicknesses ranging from 30 nm to 300 nm. UV sensitive photoresist AZ4562 [62] was spun on top of the chip with 6000 rpm for 45 seconds. The resist was baked at 115 °C for 45 seconds. After baking, the resist was exposed through the photo–mask in a mask–aligner (KarlSuss 45MA) for 30 seconds and developed for 1 minute in AZ 351B [62] developer. After developing, the opposite face of the chip was coated and baked with AZ photo–resist to prevent etching of the SiN on the that side of the chip in the next step. SiN on the exposed side of the chip was removed in RIE with CHF_3 plasma with gas flow of 50 sccm, RF power 150 W, pressure 0.073 mbar and temperature 30 °C.

The remaining SiN served as an etch mask for a crystallographic potassium hydroxide (KOH) wet–etch through the whole Si wafer thickness, producing a thin suspended SiN membrane. KOH etch was perfomed with 40% solution and at temperature 98 °C resulting to an etch rate of ∼180 µm per hour. The resulting membrane dimension and size of the window in a photo–mask for crystallographic Si(100) etch are related via relation (see Fig. 4.1).

$$L_{\mathrm{window}} = \frac{2d_{\mathrm{Si}}}{\tan(54.7°)} + L_{\mathrm{membrane}} \tag{4.1}$$

Here, L_{window} and L_{membrane} are the sizes of the side of the photo–mask window and membrane, respectively. d_{Si} is the Si wafer thickness, and the angle $54.7°$ is due to the crystallographic direction of Si [63].

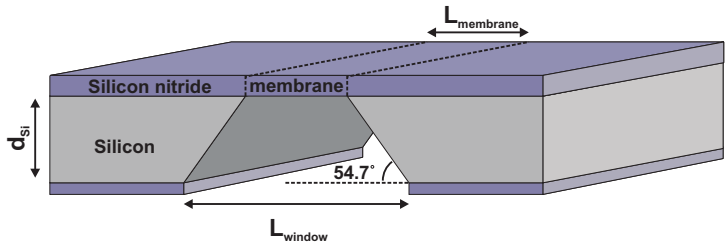

FIGURE 4.1 Schematic view of crystallographic KOH etch through the Si (100) wafer to fabricate thin silicon nitride membranes.

Metallic wires and tunnel junctions were fabricated on membranes with a similar process as described in chapter 2 using EBL and vacuum evaporation in UHV chamber. In case of suspended beams (fabricated from 30 nm thick SiN), the final structural release was perfomed by plasma etching in a RIE chamber with 50 sccm flow of CHF_3, pressure 0.1 mbar, and RF power 80 W with duration of 100 s.

4.2 Phonon transport in suspended beams

A suspended beam can be considered, at low temperatures, as a one dimensional conductor for phonons if its diameter d is smaller than the dominant thermal wavelength of phonons

$$d \leq \lambda_T = \frac{hc}{2.82 k_B T} \tag{4.2}$$

where T is temperature and c is the velocity of sound in the material. The thermal conductance in the ballistic limit can be written using Landauer formalism in the form [64]

$$G_{\mathrm{th}} = \frac{k_B^2}{h} T \sum_m \int_{x_m}^{\infty} \frac{x^2 e^x}{(e^x - 1)^2} \mathcal{T}_m(x k_B T/\hbar) \mathrm{d}x \ , \tag{4.3}$$

where $\mathcal{T}_m$ is the transmission coefficient through the beam, m is the mode number and $x_m = \hbar\omega_m(k = 0)/(k_B T)$ is the threshold energy of the mode. In the low temperature limit $k_B T < \hbar\omega_m$, only the four lowest lying modes are occupied with $x_m = 0$. The lowest occupied modes of the beam are longitudinal, torsional and two flexural modes.

Transmission through the ballistic one dimensional beam is governed by the contacts to the resevoirs [64, 57, 58]. In addition, the surface roughness of the beam can have effects on the transmission [65]. When contacts to the resevoirs have infinite catenoid shape (the edge of the contact goes as $\cosh^2(x)$) the transmission is unity ($\mathcal{T} = 1$), and Eq. (4.3) takes a simple form

$$G_0 = 4 \frac{\pi k_B^2}{6\hbar} T \ , \tag{4.4}$$

which describes the quantized thermal conductance of the wire. The prefactor $\pi k_B^2/(6\hbar)$ $= 0.9465$ pW/K^2 is called a quantum of thermal conductance. The maximum thermal conductance of each mode is $\pi k_B^2 T/(6\hbar)$ for a one dimensional nanowire with perfect contacts to the thermal resevoirs. In addition, the thermal conductance value is universal and is not dependent on particle statistics, it is the same for bosons, fermions and anyons [66]. This result has been experimentally verified for phonons by the Roukes group in Caltech in 2000 [2] and for photons by the group of Pekola in Low–temperature laboratory of TKK in 2006 [3]. For other particle species the universal thermal conductance has not been observed, yet.

However, abrupt contacts to the resevoirs complicate the simple picture discussed above and strong scattering will suppress the thermal conductance from its quantum value. In addition, the power law of temperature dependence of the thermal conductance is changed depending on the interface between the beam and the

resevoirs, causing deviation from the linear $n-1=1$ (n being the exponent for temperature dependence of the heat flow $\dot{Q}$) temperature dependence of G_{th} [57, 58]. Typically in thermal transport experiments, suspended beams are connected to resevoirs located at the bulk or on the membrane, therefore there is a difference in the phonon dimensionality at the contact. The 1D–2D scattering results in power laws $n-1=1.5$–2.5 of temperature dependence of thermal conductance [57, 58], while 1D–3D scattering results in $n-1=3$–5 [58].

4.3 Electron–phonon coupling in suspended beams

Recently, Hekking *et al.* [67] have studied electron–phonon coupling in suspended beams theoretically. In this model, the three dimensional electron gas is coupled to one dimensional phonon modes. Furthermore, electrons are assumed to couple only to longitudinal phonon modes, while the remaining three available modes have no effect on electron–phonon coupling. The resulting heat flow from electrons to phonons is [67]

$$\dot{Q}_{e-p} = \Sigma_{1D} L (T_e^3 - T_p^3) \,, \tag{4.5}$$

where Σ_{1D} is the one–dimensional electron–phonon coupling constant, L is the length of the suspended nanowire and T_e and T_p are electron and phonon temperatures, respectively. One and three dimensional electron–phonon coupling constants are related through the following relation [67]

$$\Sigma_{1D} = \frac{\pi}{6} \frac{\zeta(3)}{\zeta(5)} \left(\frac{\hbar c_l}{k_B} \right)^2 \Sigma_{3D} \,, \tag{4.6}$$

where $\zeta(x)$ is the Riemann zeta function (see e.g. [68]), c_l is the sound velocity of the longitudinal phonon mode and Σ_{3D} is the three–dimensional electron–phonon coupling constant.

4.4 Phonon cooling of suspended beams with tunnel junctions

Tunnel junction structures containing normal metal and superconducting electrodes can be used for cooling, as described in chapter 3. Typically in coolers fabricated on bulk material, only electrons are cooled below the bath temperature, while the phonon temperature remains the same as the bath due to the weakness of heat flow between electrons and phonons as limited by the electron–phonon interaction. How-

ever, several low–temperature applications would benefit from cooling both electrons and phonons. Cooling of phonons on thin SiN membranes has been demonstrated with large area SINIS structures in Refs. [69,43,60]. The possibility of cooling of phonons with SINIS structures in one dimensional beams has been suggested theoretically in Ref. [67]. Its experimental demonstration is one of the main results of this thesis [IV]. Cooling of electrons in suspended metallic beam is also reported recently in Ref. [70]. Cooling of phonon modes becomes possible, if the heat flow between electrons and phonons is not the limiting factor, but instead, phonon pathway becomes the bottleneck for thermal transport, a limit that can easily be realized by using suspended structures.

4.4.1 Sample geometry and measurement scheme

All suspended nanowires used in this thesis had a length of either 10 or 20 µm, width of 200 or 300 nm and a bilayer thickness of 60 nm, containing 30 nm Cu and 30 nm SiN. The suspended nanowire was connected to the bulk via four suspended bridges with a length of 5 µm and a width of 150 nm. The two outer bridges contained a 60 nm bilayer of Cu/SiN making the total length of the normal metal 20–30 µm, while the two inner bridges had a trilayer composition Cu/Al/SiN with a total thickness of 90 nm. Samples had two, larger area ($\sim$0.35 µm^2) NIS junctions used for cooling located either on bulk or on the suspended end of the bridge, and two small area ($\sim$0.05 µm^2) thermometer junctions located at the middle of the suspended beam. A SEM image of a sample with cooler junctions located on bulk is shown in Fig. 4.2.

All experiments were perfomed in a plastic dilution refrigerator with a base temperature of $\sim$50 mK [38]. The sample was wire bonded to the sample stage of the cryostat and connected to room temperature through carefully filtered wires. Lines from room temperature to 4.2 K were stainless steel coaxial cables, at 4.2 K was the first filter stage with low–pass filtering consisting of 1 kΩ and 1 µF surface mounted components. From 4.2 K, the wires were $\sim$1.5 m of Thermocoax cable, which filter out high frequency microwave radiation [71]. Cooler junctions had still an additional filtering at the 50 mK stage consisting of another 1 kΩ and 2.2 µF low–pass filter made out of surface mount components.

In the experiment, the temperature of the nanowire was monitored locally with small NIS thermometer junctions current biased as described in chapter 3. The DC bias voltage was slowly swept across the cooler junctions, while current and voltage of the cooler were recorded during the sweep. The measurement scheme is shown in Fig. 4.2.

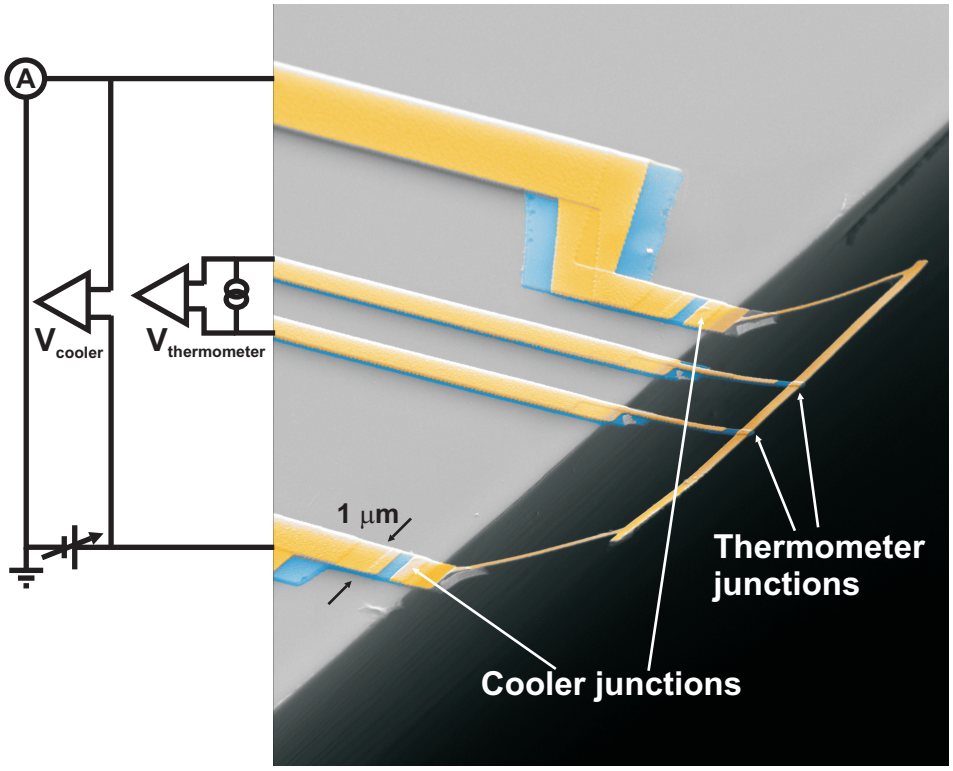

FIGURE 4.2 SEM image of suspended nanowire connected to bulk via four suspended bridges. Orange and blue colors represent copper and aluminium, respectively.

4.4.2 Cooling with different sample geometries

Two different sample geometries with cooler junctions located either on bulk or directly connected to the nanowire show completely different cooling behavior, shown in Fig. 4.3. Open circles represent data for the sample geometry where cooler junctions are directly connected to the suspended nanowire and the solid black line is the data for cooler junctions located on bulk but connected to a nanowire via bridges. The sample with cooler on bulk shows cooling from 200 mK down to 110 mK, while in the other geometry no significant cooling is observed.

The difference of the cooling behavior can be explained by reduced phonon thermal conductance of the bridges connecting the nanowire to the bulk: Hot non–equilibrium quasiparticles injected from the normal metal into the superconductor will eventually relax by emitting a phonon with energy 2Δ. If recombination phonons are created in the suspended bridges, they are very probably absorbed by the suspended nanowire, and no effective cooling is observed. However, if coolers are located on bulk, the recombination phonons are very likely absorbed by the sub-

strate, if diffusion rate of quasiparticles is large enough on the junction area. This explains the better peformance of the geometry with cooler junctions on bulk, thus, we concentrate on this geometry from now on.

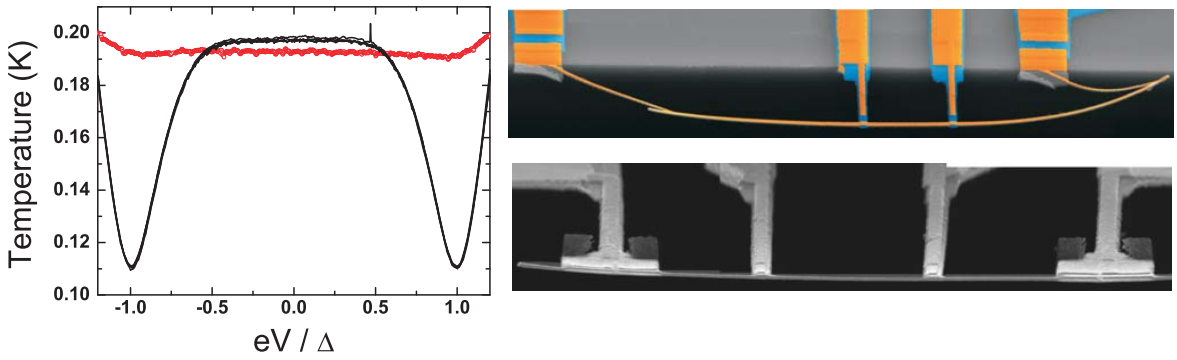

FIGURE 4.3 The plot on the left shows the difference in cooling performance of two different sample geometries. Solid line represents a geometry, where cooler junctions are located in the bulk (SEM image on top right) and open, red circles are cooling of sample with junctions located at the free standing end of the connecting bridges (SEM image on bottom right).

4.4.3 Absence of thermal gradients and charging effects

In the cooling experiments, the temperature is measured in the middle of the nanowire, while coolers are located on the bulk, separated by ∼10–15 µm from the thermometer. The separation of cooler junctions from thermometer junctions introduces the question of temperature gradients in the normal metal. Temperature gradients would lead to a non–uniform temperature profile, and therefore unequal temperatures at cooler junctions and thermometers.

The question of temperature gradients can be investigated by comparing the measured current–voltage (I–V) characteristics of cooler junctions with theoretical I–V curves parametrized with temperature. Figure 4.4(a) shows the measured and calculated I–V curves of a cooler, while (b) shows the temperature measured at the middle of the nanowire as a function of bias voltage. The cooler I–V is consistent with the lowest temperature $T = 47$ mK, which is same as measured with the thermometer. Therefore, the conclusion is that no thermal gradients develop in the nanowire and electrical thermal conductance need not be taken into account in the thermal model for samples. In addition, because of the relatively low resistivity of Cu island ($\sim 2 \cdot 10^{-8}$ Ωm), the current through the cooler does not cause significant excess heating due to power dissipation on the normal metal island.

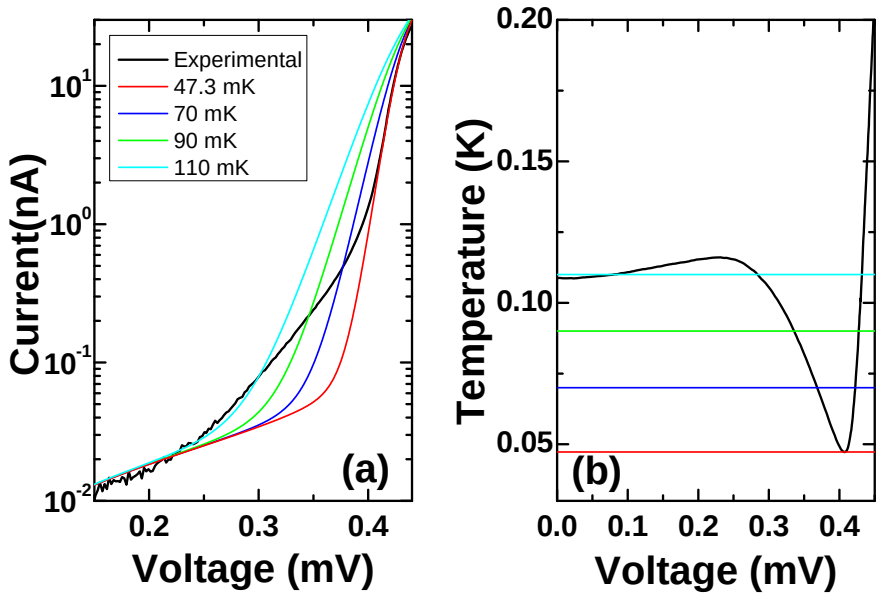

FIGURE 4.4 (a) Measured (black) I–V characteristics of cooler junctions, colored lines are calculated curves with different temperatures. (b) Temperature of the same sample measured with SINIS thermometer at the middle of the nanowire as a function of cooler bias voltage. Horizontal lines correpond the same temperatures as used in calculations in (a).

The effects of charging energy may also affect thermometry, by causing deviations from the predicted behavior (3.1) when charging energy is neglected. This might appear to be a problem especially in coolers, since temperatures reached are relatively low and hence the situation $E_C > k_B T$ can be easily reached. In addition, coolers are typically connected to the normal metal island, electrically isolated from the rest of the circuit and therefore its charging energy is dominated by the junction capacitance.

The measured Coulomb blockade of a suspended cooler at 4.2 K is presented in Fig. 4.5. By applying the weak Coulomb blockade result Eq. (2.6), the charging energy of the cooler is 20 mK, and therefore it has no effect on the thermometry and the conventional result (3.1) can be used in data analysis. The lowest temperature achieved in suspended coolers is 42 mK, two times higher than the charging energy.

4.4.4 Evidence of phonon cooling

Cooling curves of a suspended sample are shown in Fig. 4.6 measured at different bath temperatures between 50 and 600 mK. The lowest achieved temperature of the sample was 42 mK at the lowest bath temperature, corresponding to total cooling

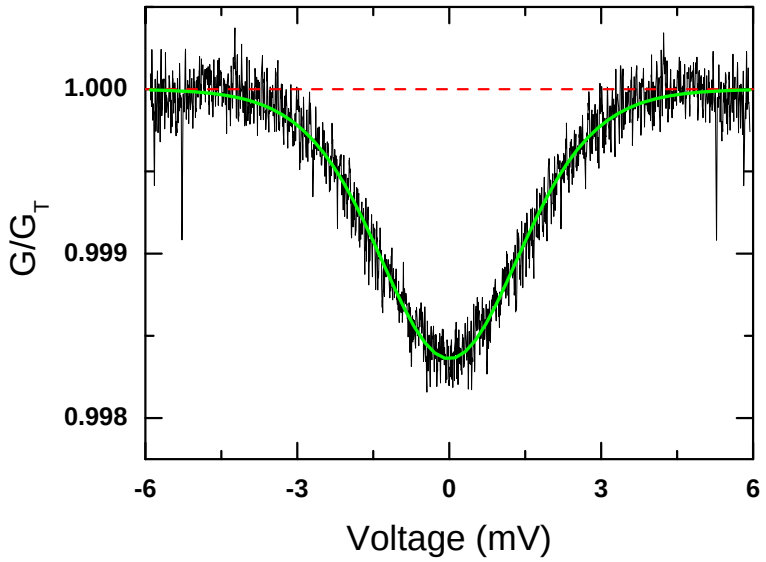

FIGURE 4.5 Measured Coulomb blockade of a suspended cooler at 4.2 K. Conductance is normalized with dashed red line G_T. Solid green line represents weak Coulomb blockade theory, Eq. (2.5).

of 60 mK, since even at the lowest bath temperature of 50 mK the nanowire temperature remains at ∼100 mK (with zero cooler bias voltage) due to noise heating via the electromagnetic environment. In addition, the sample shows cooling even at the highest bath temperature of 600 mK. The lowest temperatures (T <100 mK) are determined from the calculated voltage–to–temperature calibration of a NIS thermometer according to Eq. (3.1).

To compare with suspended coolers, samples with the same geometry and size were fabricated on a bulk substrate, where the heat flow is limited by the electron–phonon coupling. Figure 4.7 shows cooling of suspended and bulk samples with different electron gas volumes. The measurement is performed by biasing the cooler at the optimal bias point and sweeping the bath temperature. Suspended samples show better cooling (∼20% improvement at 300 mK) extending up to 600 mK (Fig. 4.7 (a) and (b)), this points out the different energy relaxation mechanisms in the bulk and suspended samples. At the very lowest temperatures (T ∼100 mK) the bulk sample in (b) shows better cooling performance due to strong decoupling of the electrons from the lattice. In addition, Fig. 4.7 shows that cooling is independent of the electron gas volume, but is dependent on the tunneling resistance R_T.

Further information about the different relaxation mechanisms between bulk and suspended structures is provided by temperature vs. cooler voltage plot Fig. 4.8. Dashed black and solid red lines represent measured values for bulk and suspended samples with $R_T = 3$ kΩ and $\Omega = 0.36$ µm^3, respectively. Open circles are calculated

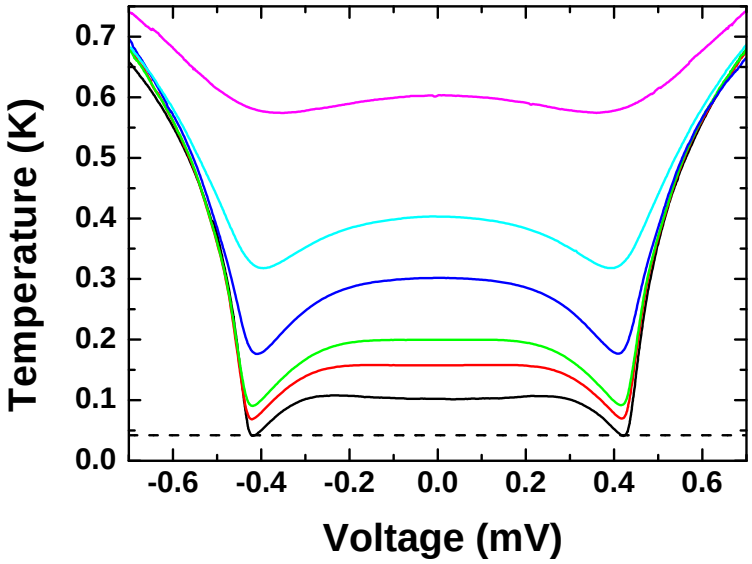

FIGURE 4.6 Measured cooler temperature vs. bias voltage for suspended sample at different bath temperatures 50, 160, 200, 300, 400 and 600 mK. Horizontal dashed line corresponds to 42 mK.

values according to Eqs. (3.8) and (3.9) with typical electron–phonon coupling parameters for Cu $n = 5$ and $\Sigma = 2.1 \cdot 10^9$ WK^{-5}m^{-3} [72,73]. Diamonds represent calculation according to 1D electron–phonon coupling model Eqs. (4.5) and (4.6) with a longitudinal sound speed of $c_l = 4900$ m/s for Cu. Calculations are performed with the assumption that phonon temperature equals bath temperature. The only fitting parameter used was $\beta = 0.03$ representing the fraction of dissipated heat flowing back to the normal metal. Clearly, 3D electron–phonon coupling can explain bulk data, but neither 3D nor 1D electron–phonon theory can fit the suspended data, and adjusting β will not improve the fit. A schematic of the thermal model is shown in Fig. 4.9. In calculations a constant heating power $P_{\mathrm{heat},\gamma}$ (typically of the order of ~ 5 fW from the electromagnetic environment) is also taken into account to fix the zero–bias temperature.

As discussed above, the observation that the magnitude of temperature decrease of the suspended nanowire is independent of the electron gas volume (nanowire length) and that the electron–phonon coupling model cannot fit the suspended data. Together with differences in cooling performance of the two different suspended geometries, this confirms the conclusion that the limiting dissipation mechanism in the suspended cooler is not electron–phonon coupling. Instead, the limiting heat flow mechanism between the nanowire and the thermal bath is the reduced thermal con-

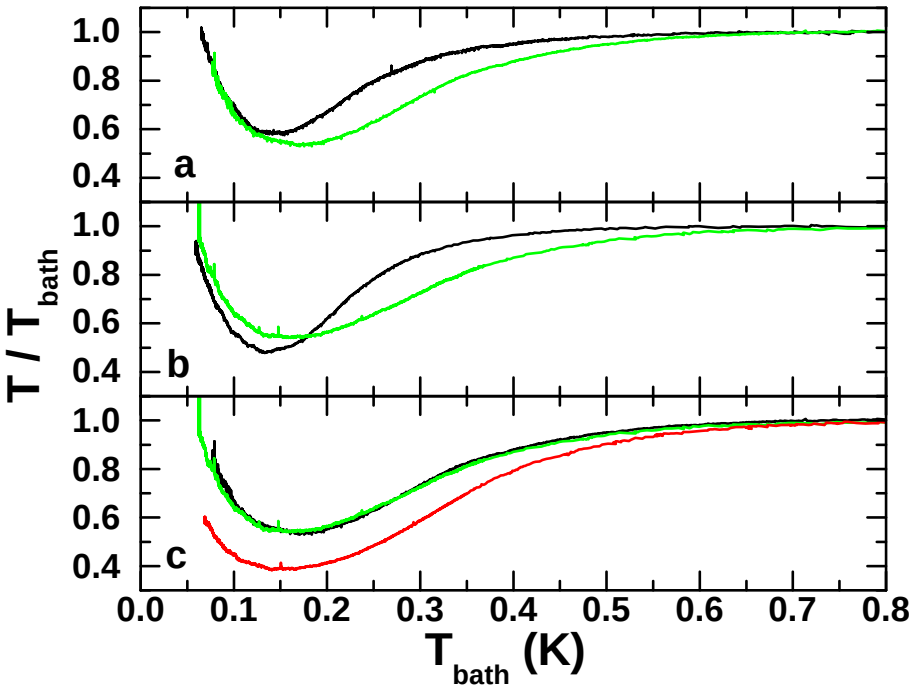

FIGURE 4.7 (a) Temperature normalized with a bath temperature T/T_{bath} of a cooled suspended $R_T = 3$ kΩ (green) and bulk $R_T = 4.4$ kΩ (black) nanowires with total length of 20 µm (electron gas volume $\Omega = 0.17$ µm^3) as a function of T_{bath}. (b) Same plot as (a) but for wires with a total length of 30 µm ($\Omega = 0.36$ µm^3) and $R_T = 3$ kΩ for both samples. (c) Comparison of cooling for two suspended samples in shown (a)(black) and (b)(green) and additional third suspended sample (red) with $R_T = 1.7$ kΩ and $\Omega = 0.36$ µm^3.

ductance due to the bridge–bulk interface. This means that heat flow is limited by phonon transmission, and that electrons and phonons are in quasiequilibrium (electron temperature equals phonon temperature) in the suspended nanowire, leading to the conclusion that cooling of electrons will provide cooling of phonons by the same amount. Therefore, the lowest phonon temperature achieved in the suspended structures is 42 mK, which is below the base temperature of the refrigerator.

To understand the transport properties, additional heat transport experiments were performed without cooler junctions but with the same nanowire width 300 nm, thickness 60 nm and length 24 µm. In this experiment, the two outer bridges had superconductor–normal metal (SN) junctions without an insulating barrier in the free–standing end of the bridges (directly connected to suspended Cu nanowire). The superconducting material for SN junctions was niobium (Nb), chosen for its relatively high critical temperature and therefore high superconducting gap. In addition, a SINIS thermometer was connected in the middle of nanowire, like in the cooler experiments. The SN junctions provide good electrical contacts, but are nearly

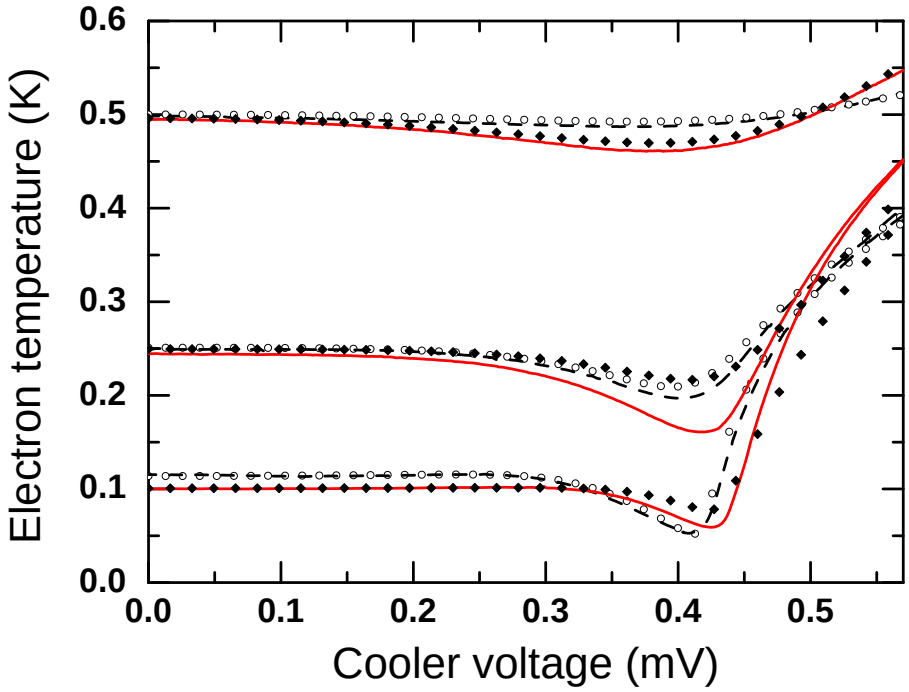

FIGURE 4.8 Measured cooler temperature vs. voltage curves for a bulk (black, dashed) and a suspended (red, solid) sample with $R_T = 3$ kΩ. Open circles and filled diamonds represent calculations using 3D and 1D electron–phonon coupling, respectively.

perfect thermal barriers because of Andreev reflection at the interface [74], and therefore Joule heating power $P_{\mathrm{in}} = IV$ in the normal metal is dissipated uniformly in the normal metal. Then $P_{\mathrm{in}} = A(T_{\mathrm{nw}}^n - T_{\mathrm{bath}}^n)$, with T_{nw} being the temperature of the nanowire. The large superconducting gap of Nb prevents sizeable heat leaks into the superconductor due to multiple Andreev reflections [75], meaning that the dissipated power within the normal metal nanowire can be accurately determined by simply measuring the current and the voltage of the SNS structure.

Figure 4.10(a) shows the result of the heating experiment, where temperature of the nanowire is plotted as a function of input power. Saturation of temperature at the lowest temperatures is due to noise heating $P_{\mathrm{heat},\gamma}$ of the electron gas (cf. Fig. 4.9). Data is well described by a transition from power law $n \sim 2.8$ at low temperatures to a power law $n \sim 6$ at high temperatures. The thermal conductance $G = \mathrm{d}P/\mathrm{d}T$ at 200 mK is 0.4 pW/K and extrapolated at 100 mK to 0.12 pW/K. Converted into units of the thermal conductance quantum according to Eq. (4.4), these values are $\sim$0.13 G_0 and 0.08 G_0 for temperatures of 200 mK and 100 mK, respectively. Values of thermal conductance can be compared with values for calculated 1D electron–phonon limited conductance, which are 5.2 pW/K and 1.3 pW/K for 200 mK and

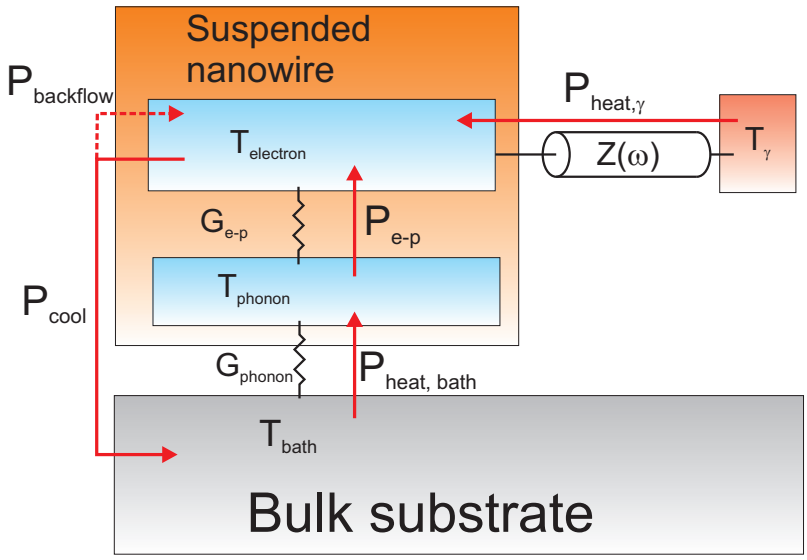

FIGURE 4.9 A schematic picture of a thermal block diagram describing the model used for calculating the electron temperature. Here, $G_{\mathrm{e-p}}$ and G_{phonon} represent thermal conductances via electron–phonon interaction and coupling of phonons of nanowire to the bath, respectively. $Z(\omega)$ represents the electrical impedance, that couples the electrons to their electromagnetic environment.

100 mK, respectively. The comparison of thermal conductances also confirms that the limiting mechanism in the heat flow is phonon mediated, since the measured thermal conductances are an order of magnitude smaller than in the case limited by electron–phonon coupling.

Measured power laws from the heating experiment can be used in the thermal model for cooler, Eqs. (3.8) and (3.9). Figure 4.10(b) shows measured cooler data (black, solid line) in comparison with the two power laws $n = 2.8$ (red, dashed line) and $n = 6$ (blue, dashed line) calculated with the thermal model. Calculated values are in good agreement with the measured data, if the transition from one power law to another is taken into account, as seen in the heating experiment. At bath temperatures $T > 0.4$ K $n = 6$ fits the experimental data well, but cannot be explained by electron–phonon coupling, since the fit parameter A is much smaller than what is expected from the theory of electron–phonon coupling. The parameter A is the same for $n = 2.8$ in both heating and cooling experiments, in contrast for the power–law $n = 6$ the value of $A = 12$ pW/K^6 is an order of magnitude smaller for the heating experiment.

The estimated cross–over of phonon dimensionality from 3D to 1D in the suspended structure takes place at around 0.4 K, since the dominant thermal wave-

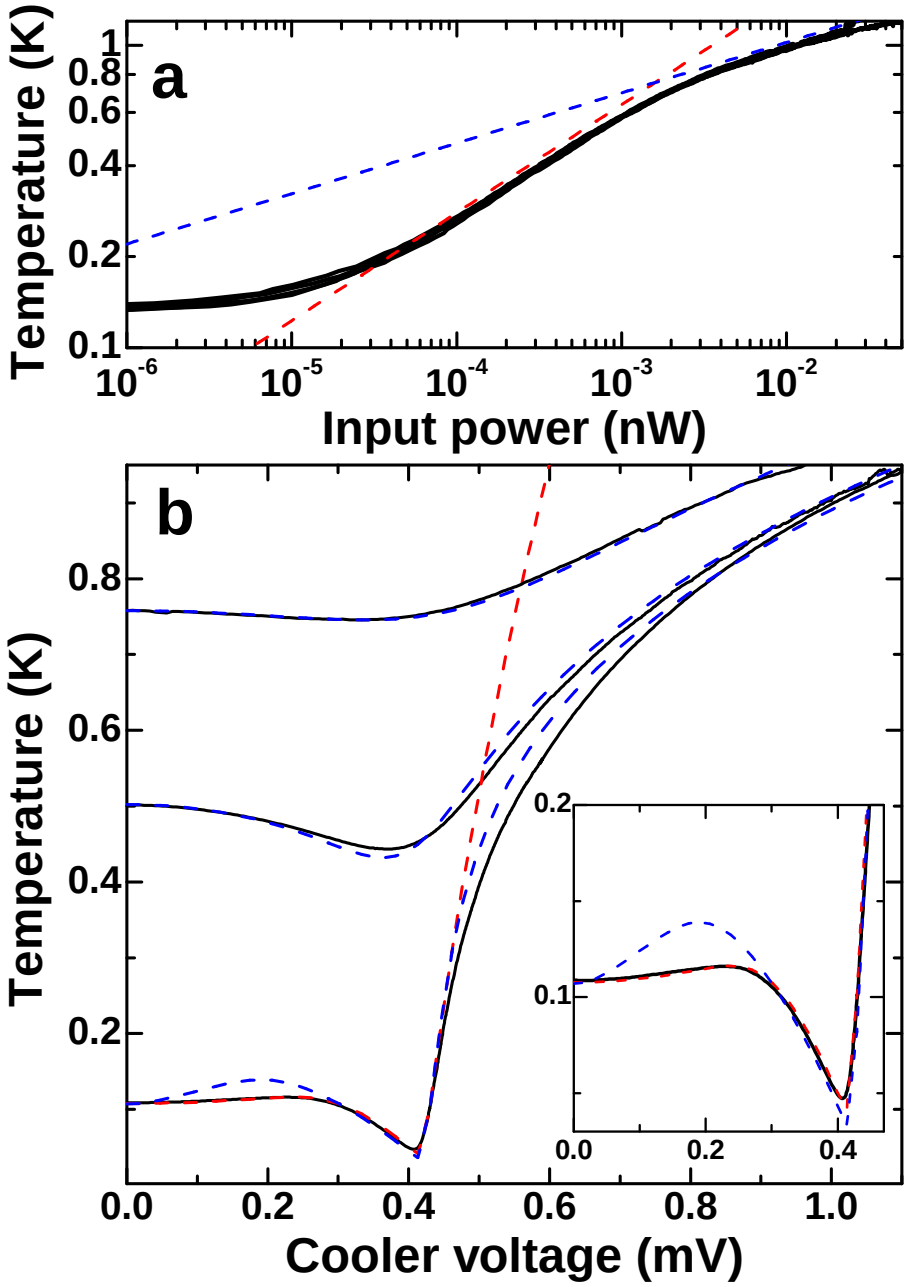

FIGURE 4.10 (a)Temperature of a nanowire as a function of dissipated power in heating experiment with SN junctions. Red dashed line and blue dashed lines correspond to power laws $n = 2.8$ and $n = 6$, respectively. (b) Temperature of a suspended nanowire as a function cooler bias voltage. Black solid line is experimental data and red and blue dashed lines correspond to power laws $n = 2.8$ and $n = 6$ calculated from thermal model, respectively. Inset represents the zoom–in to cooling region in (b). The bath temperature is 61 mK in both (a) and (b).

length (4.2) becomes larger than wire thickness, if average sound velocity $c_t = 4300$ m/s for transverse modes of the Cu/SiN bilayer is used. This is not far from the

observed transition in the experiment, and therefore phonons below temperatures 0.4 K are one dimensional. In addition, the suspended sample geometry has abrupt, non–ideal contacts to the bulk, leading to strong scattering at the bulk–bridge interface. The observed power law $n = 2.8$ is consistent with the predicted power law for boundary limited 1D–2D scattering as dicussed in section 4.2.

In conclusion, with the suspended geometry, where the cooler junctions are located on the bulk (connected to a suspended nanowire with narrow bridges), the phonon modes of the nanowire can be cooled using conventional SINIS tunnel junction coolers. The main advantages of SINIS cooling are simple operation (only DC voltage source is needed), ease of integration into nanoscale systems, compatibility with existing fabrication processes and most importantly the ability to cool both electrons and all phonon modes simultaneously. However, if the nanowire is made with much shorter length $\sim$1 µm, the 1D electron phonon coupling becomes the dominant pathway for heat transport, and hence phonon cooling becomes impossible. For example, in 1 µm long wire the electron–phonon mediated thermal conductance would be 0.2 pW/K at 200 mK, which is smaller than the observed phonon mediated thermal conductance 0.4 pW/K.

The minimum achieved temperature in structures described above was 42 mK, starting from an initial temperature of 100 mK. The limit is mostly determined by the superconducting gap of Al, since the effectiveness of cooling in a specific temperature range is strongly dependent on the value of the gap [12]. At lower temperatures, more effective cooling may be achieved with a smaller superconducting gap. Fig. 4.11 shows the calculated cooling using an additional cooler made of a material with a much lower superconducting gap $\Delta = 71$ µeV. Here, a temperature of 14 mK is achieved with an initial temperature of 45 mK. This could be achieved with the cascade cooler, where the first stage reaches 40 mK with Al. However, no experimental realization up to date exists of such a cascade cooler structure connected to a suspended nanowire.

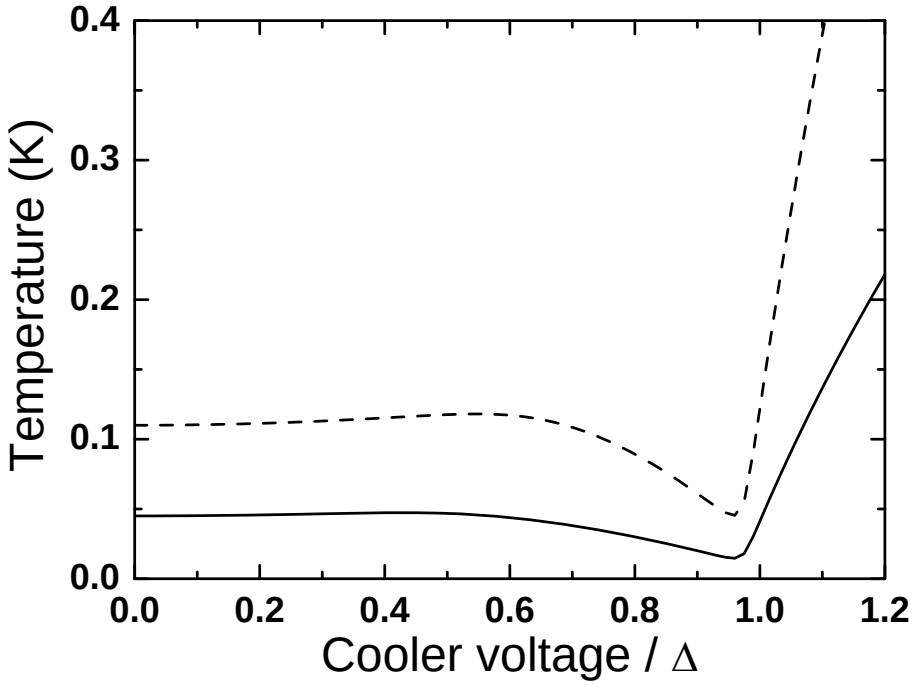

FIGURE 4.11 Calculated cooling with two different gap values $\Delta = 215$ μeV (dashed line) and $\Delta = 71.7$ μeV (solid line) for a suspended sample with thermal model used to fit the experimental data. The lowest temperature with small gap corresponds to 14 mK.

Chapter 5

Tunnel junction based strain sensing for low dimensional systems

In typical microscale applications, displacement and strain sensing is usually based on either capacitive or optical transducers. However, these methods have limitations when the dimensions of the system approach the nanoscale. For capacitive sensing, the parasitic capacitances will become overwhelmingly large compared to the capacitance of a transducer, and optical transducers will not work well because of the diffraction limit. In addition, the optical methods at sub–wavelength require sophisticated off–chip equipment.

The limitations above can be overcome with displacement sensing based on the piezoresistive effect [76, 77, 78]. Typically for nanoelectromechanical systems, piezoresistive transducers are either thin metal films or semiconductors. Some groups [79,80] have also demonstrated that magnetic tunnel junctions can be used for strain detection. However, these transducers have their own drawbacks. Semiconducting films show good responsivity, but they are typically very resistive and therefore are not very suitable for high–frequency applications due to difficulties of impedance matching. On the other hand, metal films can be made to match well to transmission lines, but they show a relatively low response to the applied strain. Although magnetic tunnel junctions show very high responses, strain sensing with magnetic tunnel junctions requires an external magnetic field, and to date, magnetic tunnel junctions for strain sensing have been relatively large in dimensions (20 µm $\times$ 20 µm or larger).

In this chapter, the feasibility of sub–micron sized normal state tunnel junctions for strain and displacement detection in nanostructures is demonstrated. The sub–micron sized tunnel junctions have several advantages in strain and displacement detection, such as their small size (dimensions can be easily made < 100 nm), existing high–frequency read–out schemes [81, 47], ease of integration into the me-

chanical system under study and a relatively good response to the applied strain. The measuring scheme for strain sensing with tunnel junctions is very simple, since only the change in the tunneling resistance of a junction needs to be measured.

5.1 Experimental details

Samples containing Al–AlO_x–Al tunnel junctions with a junction area of $\sim$0.1 μm^2 were fabricated with EBL and vacuum evaporation techniques on top of either 30 nm or 65 nm thick SiN membranes. 65 nm thick membranes were fabricated from initially 200 nm thick membranes by plasma etching in RIE with CHF_3 plasma, using recipies described in the previous chapter. After plasma thinning of the initial membrane, the final membrane thickness was verified with an ellipsometer. 30 nm thick membranes were directly fabricated from 30 nm thick LPCVD–grown SiN with wet etching techniques (cf. Chap. 4). 30 nm thick SiN membranes typically had dimensions of $\sim$120 µm $\times$ 150 µm and 65 nm membranes $\sim$250 µm $\times$ 250µm.

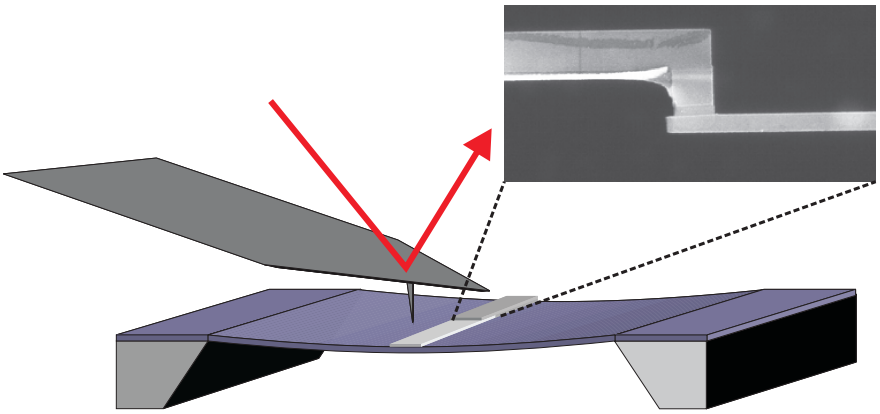

FIGURE 5.1 Schematic view of an experimental setup and zoom–in SEM image of a junction.

The membrane was actuated by an atomic force microscope (AFM) tip attached to a stiff cantilever. For the thinner membranes, OMCL-AC160TS probes from Olympus with a nominal spring constant of 42 N/m were used, and for the thicker membranes, MPP-13100 probes from Digital Instruments Veeco with a spring constant of 200 N/m were used. The actuation of the membrane was performed by pressing the membrane with a linearly increasing force sweep with a duration of 100 seconds, then holding the membrane at the maximum displacement for 60 seconds, and finally slowly releasing the membrane back to its original shape in another 100

seconds. A stiff cantilever was used to reduce the bending of the cantilever itself, and thus exerting most of the force on the membrane. A similar actuation scheme has also been used recently for thin graphene sheets [82, 83, 84]. During the actuation, the tunneling resistance, the z–piezo movement and the photo detector signal of the AFM were recorded. For each force sweep, the force vs. displacement (FZ) curves and an additional FZ curve on a hard surface were measured. The photodetector signal can be converted into displacement from the FZ curves measured on the hard surface, giving a calibration for the actual bending of the cantilever. The correct displacement of the membrane can then be calculated by substracting the bending of the cantilever from the z–piezo movement, typically the correction is of the order $\sim$200 nm. Typical maximum displacements of membranes in the vertical direction were 3–4.5 µm. A schematic of an experimental setup is shown in Fig. 5.1. All experiments were performed at room temperature and at room air. Because of the small size of the system, the direct measurement of the applied strain with an additional, calibrated strain detector was impossible. Instead, the strain fields in the membranes were calculated with a finite element method (FEM).

5.2 Modelling of a strain field

The elastic behavior of a solid can be characterized with stress and strain. Stress corresponds to the forces acting on volume elements, while strain describes the deformation of the elements. Components of the strain tensor for an elastic solid are defined with components of displacement vector **u** as [85]

$$\epsilon_{ij} = \frac{1}{2}\left(\frac{\partial u_i}{\partial x_j} + \frac{\partial u_j}{\partial x_i} + \sum_{k=1}^{3}\frac{\partial u_k}{\partial x_i}\frac{\partial u_k}{\partial x_j}\right) . \tag{5.1}$$

With small deflections (displacements), the second order terms can be neglected. The stress tensor T and strain tensor ϵ in an isotropic solid are related via the generalized Hooke's law [86]

$$T_{ij} = 2\mu\epsilon_{ij} + \lambda\sum_{k=1}^{3}\epsilon_{kk}\delta_{ij} , \tag{5.2}$$

where μ and λ are Lamé constants, which are related to Young's modulus E and Poisson ratio ν of the material through the relations [63]

$$\mu = \frac{E}{2(1+\nu)} \tag{5.3}$$

$$\lambda = \frac{E\nu}{(1-2\nu)(1+\nu)} . \tag{5.4}$$

With small deflections (displacements), the strain field can be calculated for an isotropic solid with the Navier equation [63]

$$\rho\frac{\partial^2 u_i}{\partial t^2} = \mu\nabla^2 u_i + (\mu+\lambda)\frac{\partial}{\partial x_i}(\nabla\cdot\mathbf{u}) + \mathbf{f_i}\ , \tag{5.5}$$

where ρ is the density of material and $\mathbf{f}$ is a body force (external load). However, when the mechanical system goes through large deflections, there will be two additional terms in the Navier equation and it takes the form

$$\rho\frac{\partial^2 u_i}{\partial t^2} = \mu\nabla^2 u_i + (\mu+\lambda)\frac{\partial}{\partial x_i}(\nabla\cdot\mathbf{u}) + \mathbf{f_i} + (\lambda+\mu)\sum_{j,l=1}^{3}\frac{\partial u_l^2}{\partial x_i \partial x_j}\frac{\partial u_l}{\partial x_j} + \mu\sum_{l=1}^{3}\frac{\partial u_l}{\partial x_i}\nabla^2 u_l \tag{5.6}$$

A large deflection in a membrane means that the vertical deflection z_0 is larger than the thickness τ of the membrane [85]. However, large deflections should not be confused with non–linear response or plastic, irreversible deformation of an elastic system. Even with large deflections, the response to the force can be linear, and therefore Hooke's law is valid. All experiments were performed with large deflections, since the vertical displacement is large (microns) compared to the membrane thickness, which is tens of nanometers.

Solution of the Navier equation with proper boundary conditions will provide a displacement vector. Furthermore, the strain and stress tensors can be calculated from the displacement. A SiN membrane of a finite thickness actuated at the point (x_0, y_0, τ) in the z–direction by an amount z_0 can be modelled with the following boundary conditions

$$\mathbf{u}(x = \pm L_x/2, y = \pm L_y/2, z) = 0 \tag{5.7}$$

$$\frac{\partial u_j}{\partial x_i}(\pm L_x/2, \pm L_y/2, z) = 0\ , \{j,i\} = \{1,2,3\} \tag{5.8}$$

$$\mathbf{u}(x_0, y_0, \tau) = (0, 0, -z_0)\ , \tag{5.9}$$

where $L_{x,y}$ is the length of the membrane in x and y directions and τ is the membrane thickness. The strain fields of membranes were calculated using a commercial Comsol Multiphysics sofware [87], which is a partial differential equation solver based on a finite element method (FEM) with a structural mechanics toolbox. Simulations contained a SiN membrane and tunnel junction, which was modelled as a thin Al wire on top of a membrane. Material parameters used in simulations were literature values for poly–crystalline SiN with $E = 357$ GPa and $\nu = 0.25$ and amorphous Al $E = 70$ GPa and $\nu = 0.35$ [63].

5.3 Results and discussion

The resistance of a tunnel junction and the recorded photo detector signal (force) as a function of time are shown in Fig. 5.2. The resistance is modulated by the force, and the response is reproduced and follows each force sweep.

Figure 5.3(a) shows the measured tunneling resistance response as a function of the vertical displacement of the membrane, where responses are normalized with the initial unstrained value, denoted by R_0. The actuation is performed at a distance of 1.5 µm from the junction. The lower curve is data for 30 nm thick membrane with a tunneling resistance of 9 kΩ. The top curve is data for 65 nm thick membrane with a tunneling resistance of 26 kΩ.

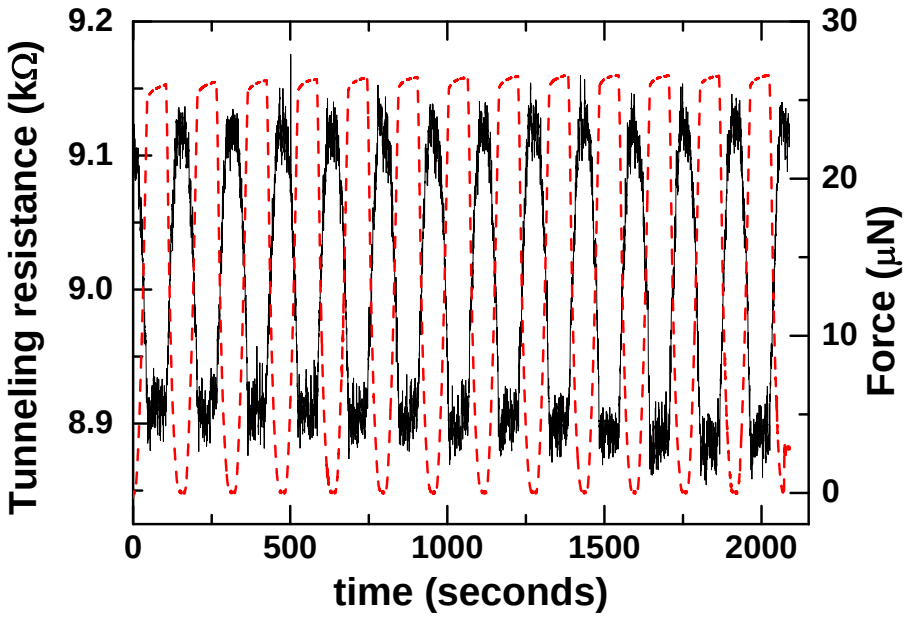

FIGURE 5.2 Tunneling resistance (black) and force (photodetector signal of the AFM) (red, dashed) as a function of time.

The response for the 30 nm thick membrane shows a clear hysteresis, while in the 65 nm data no hysteresis is observed. The hysteresis has a mechanical origin, since it can be observed also in the FZ–curves shown in Fig. 5.4 for the 30 nm data. Although the hysteresis is observed in press and release phases of the force sweep, irreversible (plastic) deformations can be ruled out, since the cycle–to–cycle behavior is non–hysteretic: In each press–release cycle, the trace and retrace of the FZ curves are reproducible and do not change from one cycle to another. The explanation for the non–hysteretic behavior of thicker membranes can be sought from the different spring constants of membranes with different thicknesses. The spring constant k of a plate has a cubic dependence on its thickness τ, i.e. $k \propto \tau^3$ [88].

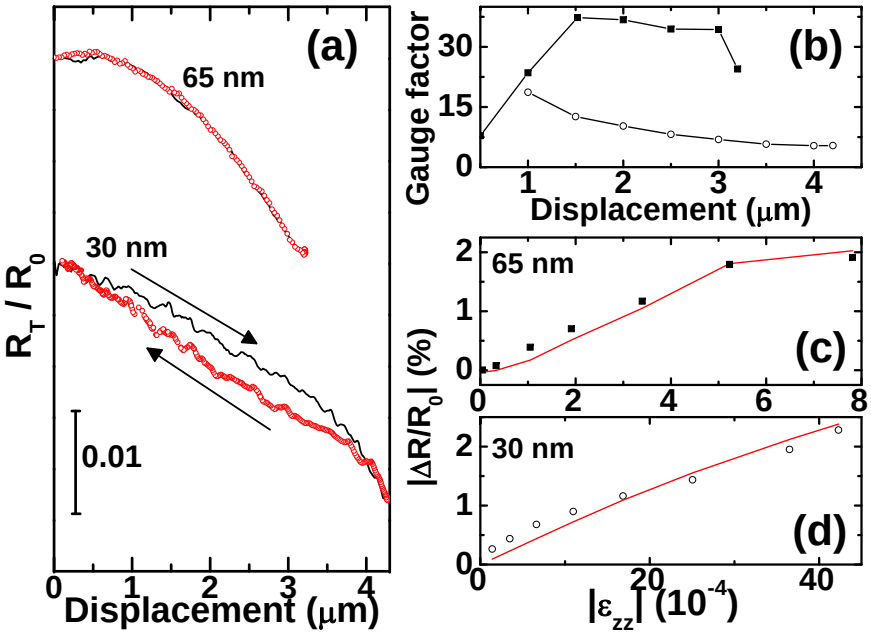

FIGURE 5.3 (a) Tunneling resistance normalized with resistance at unstrained configuration R_0 as a function of vertical deflection of a membrane. Press and release phases of a membrane are shown with black line and red open circles, respectively. Top curve is data for 65 nm thick membrane, while the bottom curve represent data for 30 nm thick membrane. (b) Calculated gauge factors as a function of displacement for 65 nm (squares) and 30 nm (open circles) membrane data, presented in (a). Relative change in the tunneling resistance vs. strain is presented in (c) for 65 nm and (d) for 30 nm data. Red lines in (c) and (d) are calculations based on Eq. (5.16).

Therefore, a 65 nm thick membrane has 10 times larger spring constant compared to a 30 nm thick membrane, and response to the applied force is one order of magnitude larger for the thinner membrane. The origin of the hysteresis may be related to the difference in the spring constants for different membrane thicknesses and the interaction between the tip and the membrane.

One figure–of–merit of a strain sensor is the gauge factor γ, defined as the ratio of relative change in the resistance to the applied strain

$$\gamma = \frac{\Delta R}{R_0}\frac{1}{\epsilon} = \frac{\tilde{R}_T - R_0}{R_0}\frac{1}{\epsilon_{zz}}\,, \tag{5.10}$$

where R_0 and $\tilde{R}_T$ are the sensor tunneling resistances at unstrained and strained configurations, respectively. Figure 5.3 (b) shows gauge factors for the 65 nm (black squares) and for the 30 nm data (open circles) presented in (a), calculated from the measured resistance response and the simulated strain field for the different vertical displacements. In the calculation of the gauge factor, the compressional strain ϵ_{zz} in

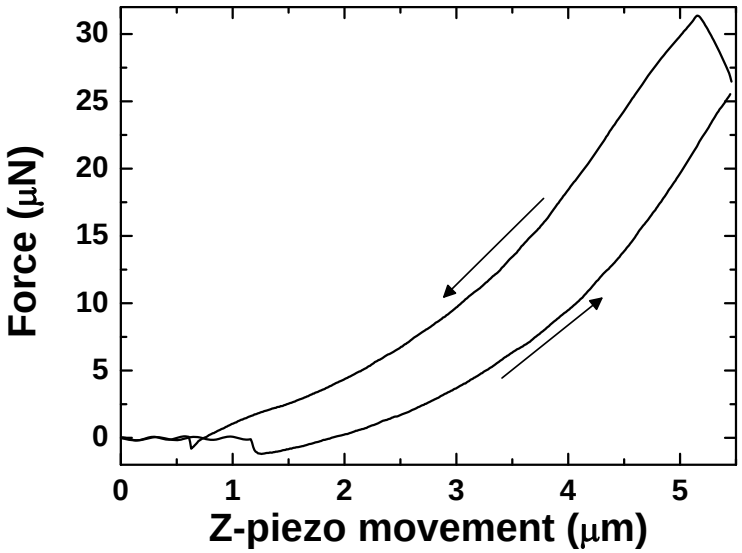

FIGURE 5.4 The force vs. displacement (photodetector signal vs. z–piezo movement) curve of the trace and the retrace data for 30 nm thick membrane.

vertical direction is used. Simulations show that the shear components are zero at the junction, if actuation is carried out right next to the junction, as in the experiment. The maximum gauge factor $\gamma \sim 37$ is obtained with a displacement of 1.5 μm and it is reduced with smaller displacements. This is much larger than typical gauge factors for metal film detectors, which are of the order of 2–4 [89].

Figures 5.3 (c) and (d) show the tunneling resistance as a function of the applied strain for the same data as in (b), calculated from the displacements in (a). (c) is data for the 65 nm membrane and (d) for the 30 nm membrane. Although the response in (a) for both samples is non–linear as a function of displacement, the response to the strain shows linear behavior due to the non–linearity between strain and displacement caused by large deflections.

An AFM can be used as a local strain actuator, as has been demonstrated with the experimental data in Fig. 5.5. Here, the membrane has been actuated by the same displacement of 3 μm at different points of the membrane. The inset shows a calculated strain field of the membrane. The actuation points are taken at the diagonal of the membrane, represented by a white dashed line. Figure 5.5 shows the measured resistance response of the tunnel junction together with the calculated strain ϵ_{zz} as a function of distance from the center of the membrane, where the tunnel junction is located. A good qualitative agreement of tunnel junction signal with the calculated strain field is achieved. Although, there are some differences between the strain field and the response of the sensor, such as response seems to be more sharply peaked than strain field and at larger distances the strain field is still 10% of the maximum,

while response of the sensor is much smaller. These differences are not yet understood.

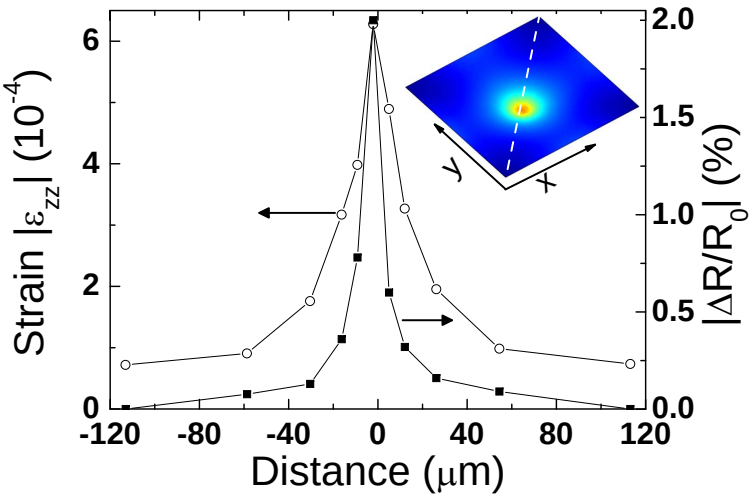

FIGURE 5.5 Measured response of a tunnel junction (black squares) and calculated strain (open circles) as a function of distance from the center of the membrane, when the membrane is actuated at different points on the diagonal. Inset shows the calculated strain field, when membrane is actuated at the middle point.

5.3.1 Simple model for response to strain dependence on junction parameters

The resistance response to the applied strain of a tunnel junction is due to deformation of the tunneling barrier. Furthermore, tunneling resistance depends exponentially on the barrier thickness and height, as presented in chapter 2. This raises an interesting question, as to whether the sensitivity and the gauge factor of a tunnel junction detector could be improved by tuning the barrier parameters e.g. by thermal annealing. The very simple model based on the Eq. (2.3) can be used to estimate the dependence of the gauge factor on the barrier parameters of a lateral tunnel junction.

The compressional strain components on the junction can be written in the form [63]

$$\epsilon_{ii} = \frac{1}{E}[T_{ii} - \nu(T_{jj} + T_{kk})] \, , \{i,j,k\} = \{x,y,z\} \, , \tag{5.11}$$

where E is the Young's modulus, ν the Poisson ratio, $T_{\{xx,yy,zz\}}$ are components of the stress tensor. The first term on the right hand side represents the strain due to applied force, while the second term is the strain component caused by the orthogonal strain components via the Poisson ratio. The tunneling resistance in the strained

configuration can be written in the form (all variables with tilde ($\sim$) represent the current quantity in the strained configuration)

$$\tilde{R}_T = \frac{h^2}{e^2\sqrt{2m\tilde{\phi}_0}}\frac{\tilde{d}}{\tilde{A}}\exp\left(\frac{2\tilde{d}}{\hbar}\sqrt{2m\tilde{\phi}_0}\right) , \tag{5.12}$$

where $\tilde{A}$ is the junction area, $\tilde{d}$ and $\tilde{\phi}_0$ are the barrier thickness and the height of the energy barrier, respectively. The junction area and thickness in the strained configuration have the form

$$\tilde{A} = A(1+\epsilon_{xx}+\epsilon_{yy}) \tag{5.13}$$

$$\tilde{d} = d(1+\epsilon_{zz}) . \tag{5.14}$$

The above equations show that the change in the tunneling resistance is mainly caused by the strain component ϵ_{zz}, which can be written in the form

$$\epsilon_{zz} = \frac{1-\nu-2\nu^2}{1-\nu}\frac{T_{zz}}{E} - \frac{\nu}{1-\nu}(\epsilon_{xx}+\epsilon_{yy}) \tag{5.15}$$

The resulting relative change in the tunneling resistance is

$$\frac{\tilde{R}_T}{R_0} - 1 = \sqrt{\frac{\phi_0}{\tilde{\phi}_0}}\frac{1+\epsilon_{zz}}{1+\epsilon_{xx}+\epsilon_{yy}}\exp\left\{\frac{2d}{\hbar}\sqrt{2m\phi_0}\left[\sqrt{\frac{\tilde{\phi}_0}{\phi_0}}(1+\epsilon_{zz})-1\right]\right\} - 1 . \tag{5.16}$$

The above expression includes the strain dependence of the barrier height (denoted as $\tilde{\phi}_0$). In semiconductors the band–gap is known to vary with the applied strain, and has the form $\Delta E_g = a(\epsilon_{xx}+\epsilon_{yy}+\epsilon_{zz})$, with value $a = -5$ eV for germanium and $a = -30$ eV for silicon [90], for example. In the calculated values of response in Fig. 5.3 (c) and (d) (red lines) the value $a = -4$ eV is used. However, the accurate values for AlO_x are not known. The quasilinear dependence of the response to the applied strain can also be explained with Eq. (5.16), since typically strain values are small $\sim 10^{-4}$ leading to small values in the exponent. The expansion of Eq. (5.16) with respect to ϵ_{zz} in the first order leads to the form

$$\frac{\tilde{R}_T}{R_0} - 1 \approx \sqrt{\frac{\phi_0}{\tilde{\phi}_0}}\frac{(1+\epsilon_{zz})(1+2d\hbar^{-1}\sqrt{2m\phi_0}\epsilon_{zz})}{1+\epsilon_{xx}+\epsilon_{yy}} - 1 . \tag{5.17}$$

Furthermore, with realistic values of the barrier parameters $d = 1.5$ nm and $\phi_0 = 1.5$ eV, it can be seen that the prefactor for the ϵ_{zz} is ~ 20, confirming that the depen-

dence on ϵ_{zz} component is dominating.

In addition, the differences in the gauge factor dependence of the displacement can be explained with this simple model: the component ϵ_{zz} depends on T_{zz} and $\epsilon_{\{xx,yy\}}$, which modify the dependence as shown in Fig. 5.6. Figure 5.6 shows gauge factors in two different cases: strains for 30 nm and 65 nm membranes, but with the same barrier parameters $d = 1.5$ nm and $\phi_0 = 1.5$ eV.

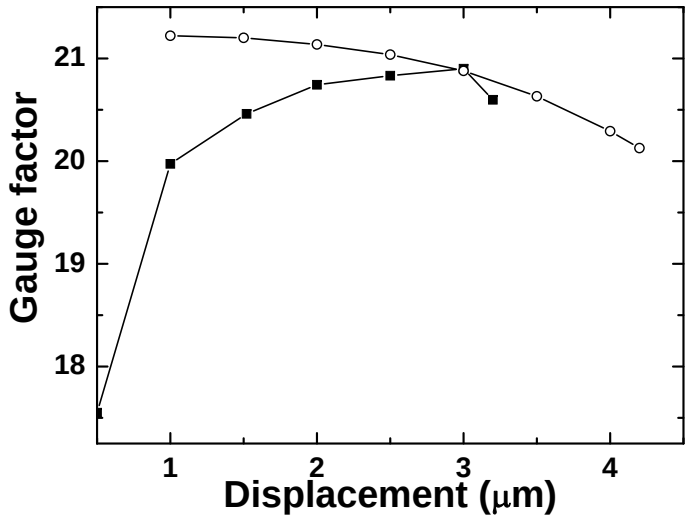

FIGURE 5.6 Calculated gauge factors with strains for 30 nm (open circles) and 65 nm membrane (black squares) with same barrier parameters.

The calculated dependence of the gauge factor as a function of junction parameters ϕ_0 and d with strains of $\epsilon_{xx} = 3.9 \cdot 10^{-4}$, $\epsilon_{yy} = 2.3 \cdot 10^{-4}$ and $\epsilon_{zz} = -5.2 \cdot 10^{-4}$, corresponding to the experiment with 65 nm membrane with a 3 μm displacement, is shown in Fig. 5.7. Different figures represent calculations with three different cases for the strain dependence of the barrier height: $\tilde{\phi}_0 = \phi_0$, (b) $\tilde{\phi}_0 = 0.995\phi_0$ and (c) $\tilde{\phi}_0 = 1.005\phi_0$. The order of magnitude of the gauge factors is consistent with the experimental values. In addition, the sign of the gauge factor changes, if the barrier height increases due to the applied strain. According to the simple model, the gauge factor could be enhanced by increasing the barrier thickness and height. According to the results in section 2.6, thermal annealing in vacuum could be one way to increase the gauge factor of a junction.

5.3.2 Displacement sensitivity of a tunnel junction

To estimate the feasibility of a tunnel junction detector for displacement sensing in nanoelectromechanical systems, let us consider a situation, where a tunnel junction is fabricated on top of a cantilever with length L and thickness τ. The maximum

vertical displacement of a cantilever is obtained at the end of the cantilever, and it has the form [63]

$$u_{z,\max} = -\epsilon_{zz}\left(\frac{L^2}{\nu\tau} + \frac{\tau}{4}\right) . \tag{5.18}$$

The above relation allows to estimate the position sensitivity of the tunnel junction detector on the cantilever: The maximum gauge factor in the experiments above was $\gamma = 37$, resistance sensitivity of the measurement setup can be improved to be $\Delta R/R = 10^{-6}$, reached with commercially available electronics. The resistance sensitivity is $2.7 \cdot 10^{-5}$ with the current lock–in setup, used in the experiments above. Values of γ and resistance sensitivity of 10^{-6} yield the strain sensitivity of $\epsilon_{zz} = 2.7 \cdot 10^{-8}$. Substituting the strain sensitivity to Eq. (5.18) results in $u_{z,\max} = 1$ pm with cantilever dimensions of $L = 1$ µm and $\tau = 100$ nm.

The case above however, is calculated in the static situation. The case of vibrating cantilever is much more interesting, when considering real NEMS applications. With a vibrating cantilever the position sensitivity may be different than in the static case, since sensitivity depends e.g. on the effectiveness of the impedance matching between the transducer and the read–out circuitry at high frequencies.

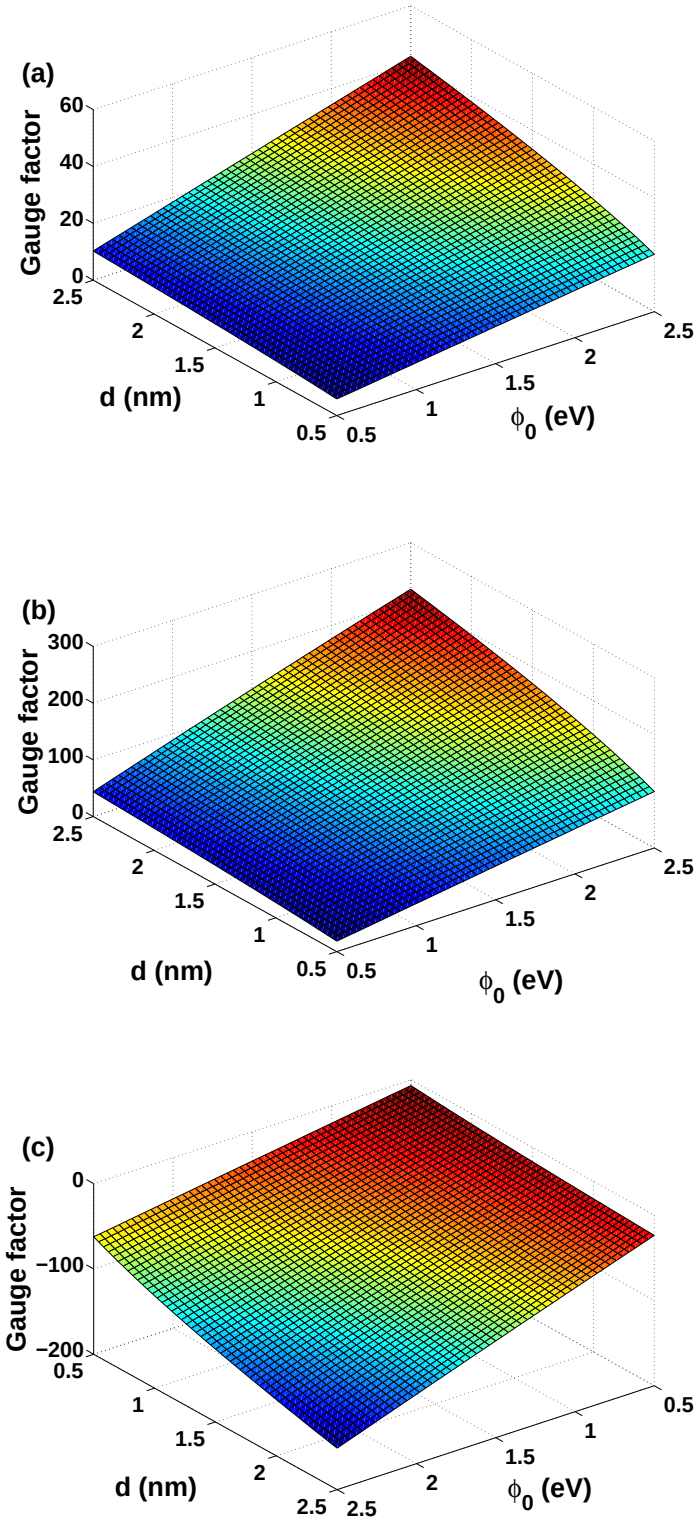

FIGURE 5.7 Calculated gauge factors as a function of barrier height ϕ_0 and thickness d with $\nu = 0.25$ and $\epsilon_{xx} = 3.9 \cdot 10^{-4}$, $\epsilon_{yy} = 2.3 \cdot 10^{-4}$ and $\epsilon_{zz} = -5.2 \cdot 10^{-4}$, typical values for 65 nm thick membrane. (a) $\tilde{\phi}_0 = \phi_0$, (b) $\tilde{\phi}_0 = 0.995\phi_0$ and (c) $\tilde{\phi}_0 = 1.005\phi_0$.

Chapter 6

Summary

The properties of AlO_x based tunnel junctions can be improved with thermal annealing in vacuum at 350–450 °C, as shown in chapter 2. A proper annealing treatment will lead to the complete stabilization of the junctions, and additionally the tunnel barrier quality improves, manifested by a diappearance of the spurious resonances in the tunneling conductance spectrum. The tunneling resistance and the charging energy increase in the annealing procedure, while the switching current is reduced, consistent with the increase of the resistance. In addition, the film quality of Al was improved upon annealing, showing an increase in the mean free path from 7.7 to 12 nm.

The stabilization of junctions is an obvious advantage when considering practical and commercial applications of tunnel junction devices. However, engineering the sample parameters in a controlled way with vacuum annealing is not yet possible, partly because a microscopic understanding of the processes is still lacking. One possible application for the annealing is to increase the sensitivity of current threshold detectors based on Josephson junctions, used for example in superconducting qubit readouts [91] or in shot noise measurements [92]. Additionally, annealing of NIS junctions could be beneficial in cooling and thermometry due to a possible reduction of the sub–gap current. However, annealing treatment was not successful with conventional Cu based junctions. For future prospects, studies on the influence of thermal annealing on 1/f noise of the junctions would be beneficial. Since thermal annealing is observed to heal the barrier, it could also reduce the amount of two level systems in the barrier and therefore lead to a reduction of 1/f noise in the junction. Low frequency 1/f noise is known to be one source of decoherence in tunnel junction based qubits [93], and therefore the reduction of noise could improve the decoherence time.

Chapter 3 introduced normal metal–insulator–superconductor based tunnel junctions for thermometry and cooling. Charging effects change the shape of the

voltage–to–temperature response of a current biased thermometer. Therefore, in a typical solitary thermometer these effects should be taken into account in the voltage to temperature conversion (calibration). In typical coolers however, the charging energy is ~ 20 mK and the calibration of a thermometer attached to the normal metal island of a cooler can be carried out in a convetional way, even at the very lowest temperatures achieved in our suspended setup. In addition, with an additional gate electrode the responsivity of a thermometer can be modulated, having its maximum responsivity with a closed gate configuration (maximal Coulomb blockade).

Electronic cooling of phonon modes of a suspended nanowire was demonstrated in chapter 4. To minimize the backflow of heat, the cooler junctions should be located on the bulk and connected to the nanowire via free standing bridges. The heat flow between the nanowire and the bulk in suspended samples was limited by a scattering of phonons at the nanowire–bulk contact. The lowest temperature achieved in suspended samples was 42 mK, starting from a temperature of 100 mK. In addition, the comparison between suspended and bulk samples showed better cooling performance up to much higher temperatures in the suspended structures.

The advantages of tunnel junction based coolers are ease of integration into a nanoscale system, compatibility with existing fabrication processes, DC operation and the ability to cool down both electrons and phonons simultaneously. Cooling of both electrons and phonons is beneficial to nanoscale bolometric applications. The noise–equivalent–power of bolometers depends not only on electron temperature, but also on phonon temperature, and therefore cooling down both will improve performance. In addition, the suitability of tunnel junction based cooling for nanomechanical systems to their ground states can be envisioned. Studies of nanomechanical systems at the quantum limit would benefit from cooling down electrons and all thermally occupied phonon modes. The decoherence of mechanical superposition states could be improved by having all thermal systems (electrons and different phonon modes) in equilibrium, instead of each system having their own temperature. Typically, back–action cooling [94,95] of a nanomechanical resonator only cools down a single, particular mechanical mode instead of all phonon modes. However, a drawback for cooling nanomechanical systems with tunnel junctions is the fact that bridges are needed to limit the thermal conductivity. Such bottlenecks can easily limit the quality factors and resonance frequencies of nanomechanical resonators. However, temperature ranges achieved with tunnel junction coolers are promising for the cooling of nanomechanical systems into their ground states, since e.g. for a 1 GHz resonator, 42 mK corresponds to occupation number $N = 1$.

Normal state, sub–micron sized tunnel junctions can be used for strain sensing in nanostructures, as demonstrated in chapter 5. Tunnel junction based strain detec-

tors show competitive gauge factors compared to metal film detectors, and they are easy to integrate into the mechanical system under study. Measurement schemes for the strain and displacement sensing with tunnel junctions are relatively simple, since only the measurement of the tunneling resistance is needed. In addition, existence of high frequency read–out schemes increase the feasibility of tunnel junction based detectors for nanoelectromechanical systems.

Bibliography

[I] This thesis article **B.I.**

[II] This thesis article **B.II.**

[III] This thesis article **B.III.**

[IV] This thesis article **B.IV.**

[V] This thesis article **B.V.**

[VI] This thesis article **B.VI.**

[1] FERRY, D. K. AND GOODNICK, S. M., *Transport in Nanostructures* (Cambridge, Cambridge, UK, 2001).

[2] SCHWAB, K., HENRIKSEN, E. A., WORLOCK, J. M., AND ROUKES, M. L., *Measurement of the quantum of thermal conductance*. Nature **404** (2000) 974–977.

[3] MESCHKE, M., GUICHARD, W., AND PEKOLA, J. P., *Single-mode heat conduction by photons*. Nature **444** (2006) 187–190.

[4] KARVONEN, J. T. AND MAASILTA, I. J., *Influence of phonon dimensionality on electron energy relaxation*. Phys. Rev. Lett. **99** (2007) 145503.

[5] ROUKES, M. L., *Yoctocalorimetry: Phonon counting in nanostructures*. Physica B **263–264** (1999) 1–15.

[6] SCHWAB, K. C. AND ROUKES, M. L., *Putting mechanics into quantum mechanics*. Phys. Today **58** (2005) 36–42.

[7] KNOBEL, R. G. AND CLELAND, A. N., *Nanometre–scale displacement sensing using a single electron transistor*. Nature **424** (2004) 291–293.

[8] LI, M., TANG, H., AND ROUKES, M. L., *Ultra–sensitive NEMS–based cantilevers for sensing, scanned probe and very high–frequency applications*. Nature Nanotechnology **2** (2007) 114–120.

[9] RUGAR, D., BUDAKIAN, R., MAMIN, H. J., AND CHUI, B. W., *Single spin detection by magnetic resonance force microscopy*. Nature **430** (2004) 329–332.

[10] YANG, Y. T., CALLEGARI, C., FENG, X. L., EKINCI, K. L., AND ROUKES, M. L., *Zeptogram–scale nanomechanical mass sensing*. Nano Lett. **6** (2006) 583–586.

[11] ENSS, C. (ed.), *Cryogenic Particle Detection* (Springer, Berlin, Germany, 2005).

[12] GIAZOTTO, F., HEIKKILÄ, T. T., LUUKANEN, A., SAVIN, A. M., AND PEKOLA, J. P., *Opportunities for mesoscopics in thermometry and refrigeration: Physics and applications*. Rev. Mod. Phys. **78** (2006) 217–274.

[13] DUZER, T. V. AND TURNER, C. W., *Principles of Superconductive Devices and Circuits* (Prentice Hall, Upper Saddle River, New Jersey, 1999).

[14] GRABERT, H. AND DEVORET, M. (eds.), *Single Charge Tunneling: Coulomb Blockade Phenomena In Nanostructures*, NATO ASI Series (Plenum, New York, 1992).

[15] MOODERA, J. S., KINDER, L. R., WONG, T. M., AND MESERVEY, R., *Large magnetoresistance at room temperature in ferromagnetic thin film tunnel junctions*. Phys. Rev. Lett. **74** (1995) 3273–3276.

[16] DEVORET, M. H. AND MARTINIS, J. M., *Implementing qubits with superconducting integrated circuits*. Quant. Info. Proc. **3** (2004) 163–203.

[17] PEKOLA, J. P., ANGHEL, D. V., SUPPULA, T. I., SUOKNUUTI, J. K., MANNINEN, A. J., AND MANNINEN, M., *Trapping of quasiparticles of a nonequilibrium superconductor*. Appl. Phys. Lett. **76** (2000) 2782–2784.

[18] GLOOS, K., KOPPINEN, P. J., AND PEKOLA, J. P., *Properties of native ultrathin aluminum oxide tunnel barriers*. J. Phys.: Condens. Matter **15** (2003) 1733–1746.

[19] WOLF, E. L., *Principles of electron tunneling spectroscopy* (Oxford, New York, 1985).

[20] MESSIAH, A., *Quantum Mechanics* (John Wiley & Sons, New York, 1958).

[21] SIMMONS, J. G., *Generalized formula for the electric tunnel effect between similar electrodes separated by a thin insulating film*. J. Appl. Phys. **34** (1963) 1793–1803.

[22] XU, Y.-N. AND CHING, W. Y., *Self-consistent band structures, charge distributions, and optical-absorption spectra in MgO, a-Al_2O_3, and $MgAl_2O_4$*. Phys. Rev. B **43** (1991) 4461–4472.

[23] RIPPARD, W. H., PERRELLA, A. C., ALBERT, F. J., AND BUHRMAN, R. A., *Ultrathin aluminum oxide tunnel barriers*. Phys. Rev. Lett. **88** (2002) 046805.

[24] PEKOLA, J., HIRVI, K., KAUPPINEN, J., AND PAALANEN, M., *Thermometry by arrays of tunnel junctions*. Phys. Rev. Lett. **73** (1994) 2903–2906.

[25] TINKHAM, M., *Introduction to Superconductivity* (McGraw–Hill, New York, 1996), 2nd ed.

[26] DYNES, R. C., NARAYANAMURTI, V., AND GARNO, J. P., *Direct measurement of quasiparticle–lifetime broadening in a strong–coupled superconductor*. Phys. Rev. Lett. **41** (1978) 1509–1512.

[27] DYNES, R. C., GARNO, J. P., HERTEL, G. B., AND ORLANDO, T. P., *Tunneling study of superconductivity near the metal–insulator transition*. Phys. Rev. Lett. **53** (1984) 2437–2440.

[28] PEKOLA, J. P., HEIKKILÄ, T. T., SAVIN, A. M., FLYKTMAN, J. T., GIAZOTTO, F., AND HEKKING, F. W. J., *Limitations in cooling electrons using normal–metal–superconductor tunnel junctions*. Phys. Rev. Lett. **92** (2004) 056804.

[29] O'NEIL, G. C., SCHMIDT, D. R., MILLER, N. A., ULLOM, J. N., IRWIN, K. D., WILLIAMS, A., ARNOLD, G. B., AND RUGGIERO, S. T., *Progress in density of states measurements of Al lightly doped with Mn*. J. Low Temp. Phys. **151** (2008) 70–75.

[30] TOPPARI, J. J., KÜHN, T., HALVARI, A. P., AND PARAOANU, G. S., *Method for finding the critical temperature of the island in a SET structure*. J. Phys.: Conf. Ser. **150** (2009) 022088.

[31] HEKKING, F. W. J. AND NAZAROV, Y. V., *Subgap conductivity of a superconductor–normal–metal tunnel interface*. Phys. Rev. B **49** (1994) 6847–6852.

[32] RAJAURIA, S., GANDIT, P., FOURNIER, T., HEKKING, F. W. J., PANNETIER, B., AND COURTOIS, H., *Andreev current-induced dissipation in a hybrid superconducting tunnel junction*. Phys. Rev. Lett. **100** (2008) 207002.

[33] JOSEPHSON, B. D., *Possible new effects in superconductive tunnelling*. Phys. Lett. **1** (1962) 251–253.

[34] AMBEGAOKAR, V. AND BARATOFF, A., *Tunneling between superconductors*. Phys. Rev. Lett. **10** (1963) 486–489.

[35] NAHUM, M. AND MARTINIS, J. M., *Ultrasensitive-hot-electron microbolometer*. Appl. Phys. Lett. **63** (1993) 3075–3077.

[36] TAN, E., MATHER, P. G., PERRELLA, A. C., READ, J. C., AND BUHRMAN, R. A., *Oxygen stoichiometry and instability in aluminum oxide tunnel barrier layers*. Phys. Rev. B **71** (2005) 161401(R).

[37] Boralectric®heaters are supplied by Tectra Physikalische Instrumente GmbH (www.tectra.de) and manufactured by Momentive Ltd. (www.advceramics.com).

[38] PEKOLA, J. AND KAUPPINEN, J., *Insertable dilution refrigerator for characterization of mesoscopic samples*. Cryogenics **34** (1994) 843–845.

[39] HOLST, T., ESTEVE, D., URBINA, C., AND DEVORET, M. H., *Effect of a transmission line resonator on a small capacitance tunnel junction*. Phys. Rev. Lett. **73** (1994) 3455–3458.

[40] KIVIOJA, J., *Mesoscopic superconducting tunnel junction devices: Experimental Studies of Performance Limitations*, Ph.D. thesis, Helsinki University of Technology (2005).

[41] JOYEZ, P., LAFARGE, P., FILIPE, A., ESTEVE, D., AND DEVORET, M. H., *Observation of parity-induced suppression of Josephson tunneling in the superconducting single electron transistor*. Phys. Rev. Lett. **72** (1994) 2458–2461.

[42] LEIVO, M. M., PEKOLA, J. P., AND AVERIN, D., *Efficient peltier refrigeration by a pair of normal metal/insulator/superconductor junctions*. Appl. Phys. Lett. **68** (1996) 1996–1998.

[43] CLARK, A. M., MILLER, A. N., WILLIAMS, A., RUGGIERO, S. T., HILTON, G. C., VALE, L. R., BEALL, J. A., IRWIN, K. D., AND ULLOM, J. N., *Cooling of bulk material by electron-tunneling refrigerators*. Appl. Phys. Lett. **86** (2005) 173508.

[44] YUNG, C. S., SCHMIDT, D. R., AND CLELAND, A. N., *Thermal conductance and electron-phonon coupling in mechanically suspended nanostructures*. Appl. Phys. Lett. **81** (2002) 31–33.

[45] ROWELL, J. M. AND TSUI, D. C., *Hot electron temperature in InAs measured by tunneling*. Phys. Rev. B **14** (1976) 2456–2463.

[46] KAUTZ, R. L., ZIMMERLI, G., AND MARTINIS, J. M., *Self-heating in the coulomb-blockade electrometer*. J. Appl. Phys. **73** (1993) 2386–2396.

[47] SCHMIDT, D. R., YUNG, C. S., AND CLELAND, A. N., *Nanoscale radio-frequency thermometry*. Appl. Phys. Lett. **83** (2003) 1002–1004.

[48] SAIRA, O.-P., MESCHKE, M., GIAZOTTO, F., SAVIN, A. M., MÖTTÖNEN, M., AND PEKOLA, J. P., *Heat transistor: Demonstration of gate–controlled electronic refrigeration*. Phys. Rev. Lett. **99** (2007) 027203.

[49] PEKOLA, J. P., VARTIAINEN, J. J., MÖTTÖNEN, M., SAIRA, O.-P., MESCHKE, M., AND AVERIN, D. V., *Hybrid single-electron transistor as a source of quantized electric current*. Nature Phys. **4** (2008) 120.

[50] KEMPPINEN, A., MESCHKE, M., MÖTTÖNEN, M., AVERIN, D. V., AND PEKOLA, J. P., *Quantized current of a hybrid single-electron transistor with superconducting leads and a normal-metal island*. arXiv:0803.1563 (2008).

[51] REICHL, L. E., *A modern course in statistical physics* (John Wiley & Sons, New York, 1998), 2nd ed.

[52] ANDERSON, M. H., ENSHER, J. R., MATTHEWS, M. R., WIEMAN, C. E., AND CORNELL, E. A., *Observation of Bose–Einstein condensation in a dilute atomic vapor*. Science **269** (1995) 198–201.

[53] JOCHUM, J., MEARS, C., GOLWALA, S., SADOULET, B., CASTLE, J. P., CUNNINGHAM, M. F., DURY, O. B., FRANK, M., LABOV, S. E., LIPSCHULTZ, F. P., NETEL, H., AND NEUHAUSER, B., *Modelling the power flow in normal conductor–insulator–superconductor jnuctions*. J. Appl. Phys. **83** (1998) 3217–3224.

[54] FISHER, P. A., ULLOM, J. N., AND NAHUM, M., *High–power on–chip microrefrigerator based on a normal–metal/insulator/superconductor tunnel junction*. Appl. Phys. Lett. **74** (1999) 2705–2707.

[55] SERGEEV, A. V. AND MITIN, V., *Electron–phonon interaction in disordered conductors: Static and vibrating scattering potentials*. Phys. Rev. B **61** (2000) 6041–6047.

[56] KÜHN, T. AND MAASILTA, I. J., *Maximizing phonon thermal conductance for ballistic membranes*. J. Phys.: Conf. Ser. **92** (2007) 012082.

[57] CROSS, M. C. AND LIFSHITZ, R., *Elastic wave transmission at an abrupt junction in a thin plate with application to heat transport and vibrations in mesoscopic systems*. Phys.Rev. B **64** (2001) 085324.

[58] CHANG, C.-M. AND GELLER, M. R., *Mesoscopic phonon transmission through a nanowire-bulk contact*. Phys. Rev. B **71** (2005) 125304.

[59] NAHUM, M., ELLES, T. M., AND MARTINIS, J. M., *Electronic microrefrigerator based on a normal–insulator–superconductor tunnel junction*. Appl. Phys. Lett. **65** (1994) 3123–3125.

[60] MILLER, N. A., O'NEIL, G. C., BEALL, J. A., HILTON, G. C., IRWIN, K. D., SCHMIDT, D. R., VALE, L. R., AND ULLOM, J. N., *High resolution x-ray transition-edge sensor cooled by tunnel junction refrigerators*. Appl. Phys. Lett. **92** (2008) 163501.

[61] Microfabrication Laboratory, University of California at Berkeley, microlab.berkeley.edu.

[62] AZ Electronic Material Ltd., www.az–em.com.

[63] CLELAND, A. N., *Foundations of Nanomechanics* (Springer, New York, 2003).

[64] REGO, L. G. C. AND KIRCZENOW, G., *Quantized thermal conductance of dielectric quantum wires*. Phys. Rev. Lett. **81** (1998) 232–235.

[65] SANTAMORE, D. H. AND CROSS, M. C., *Effect of surface roughness on the universal thermal conductance*. Phys. Rev. B **63** (2001) 184306.

[66] BLENCOWE, M., *Quantum electromechanical systems*. Phys. Rep. **395** (2004) 159–222.

[67] HEKKING, F. W. J., NISKANEN, A. O., AND PEKOLA, J. P., *Electron–phonon coupling and longitudinal mechanical–mode cooling in a metallic nanowire*. Phys. Rev. B **77** (2008) 033401.

[68] SPIEGEL, M. R. AND LIU, J., *Mathematical handbook of formulas and tables* (McGraw–hill, New York, 1999), 2nd ed.

[69] LUUKANEN, A., LEIVO, M. M., SUOKNUUTI, J. K., MANNINEN, A. J., AND PEKOLA, J. P., *On-chip refrigeration by evaporation of hot electrons at sub–kelvin temperatures*. J. Low Temp. Phys. **120** (2000) 281–290.

[70] MUHONEN, J. T., NISKANEN, A. O., MESCHKE, M., PASHKIN, Y. A., TSAI, J. S., SAINIEMI, L., FRANSSILA, S., AND PEKOLA, J. P., *Electronic cooling of a submicron–sized metallic beam*. Appl. Phys. Lett. **94** (2009) 073101.

[71] ZORIN, A. B., *The thermocoax cable as the microwave frequency filter for single electron circuits*. Rev. Sci. Instrum. **66** (1995) 4296–4300.

[72] ROUKES, M. L., FREEMAN, M. R., GERMAIN, R. S., RICHARDSON, R. C., AND KETCHEN, M. B., *Hot electrons and energy transport in metals at millikelvin temperatures*. Phys. Rev. Lett. **55** (1985) 422–425.

[73] KARVONEN, J. T., TASKINEN, L. J., AND MAASILTA, I. J., *Influence of temperature gradients on tunnel junction thermometry below 1K: cooling and electron-phonon coupling*. J. Low Temp. Phys. **149** (2007) 121–135.

[74] BLONDER, G. E., TINKHAM, M., AND KLAPWIJK, T. M., *Transition from metallic to tunneling regimes in superconducting microstrictions: Excess current, charge imbalance and supercurrent conversion*. Phys. Rev. B **25** (1982) 4515–4532.

[75] HOFFMANN, C., LEFLOCH, F., AND SANQUER, M., *Inelastic relaxation and noise temperature in S/N/S junctions*. Eur. Phys. J. B **29** (2002) 629–633.

[76] KUCZYNSKI, G. C., *Effect of elastic strain on the electrical resistance of metals*. Phys. Rev. **94** (1954) 61–64.

[77] SMITH, C. S., *Piezoresistance effect in germanium and silicon*. Phys. Rev. **94** (1954) 42–49.

[78] PARKER, R. L. AND KRINSKY, A., *Electrical resistance–strain characteristics of thin evaporated metal films*. J. Appl. Phys. **34** (1963) 2700–2708.

[79] LÖHNDORF, M., DUENAS, T., TEWES, M., AND. M. RÜHRIG, E. Q., AND WECKER, J., *Highly sensitive strain sensors based on a magnetic tunnel junctions*. Appl. Phys. Lett. **81** (2002) 313.

[80] JEN, S. U., CHEN, Y.-T., WU, J.-M., CHEN, W.-C., CHENG, W.-C., AND YAO, Y. D., *The straining effect on tunneling resistance of Co/AlO_x/Co/IrMn junctions*. Appl. Phys. Lett. **89** (2006) 222510.

[81] SCHOELKOPF, R. J., WAHLGREN, P., KOZHEVNIKOV, A. A., DELSING, P., AND PROBER, D. E., *The radio-frequency single-electron transistor (RF–SET): A fast and ultrasensitive electrometer*. Science **280** (1998) 1238–1242.

[82] LEE, C., WEI, X., KYSAR, J. W., AND HONE, J., *Measurement of the elastic properties and intrinsic strenght of monolayer graphene*. Science **321** (2008) 385–388.

[83] POOT, M. AND VAN DER ZANT, H. S. J., *Nanomechanical properties of few–layer graphene membranes*. Appl. Phys. Lett. **92** (2008) 063111.

[84] FRANK, I. W., TANENBAUM, D. M., VAN DER ZANDE, A. M., AND MCEUEN, P. L., *Mechanical properties of suspended graphene sheets*. J. Vac. Sci. Technol. B **25** (2007) 228–2561.

[85] LANDAU, L. D. AND LIFSHITZ, E. M., *Theory of elasticity* (Pergamon Press, Oxford, 1970), 2nd ed.

[86] PELESKO, J. A. AND BERNSTEIN, D. H., *Modeling MEMS and NEMS* (Chapman & Hall, Boca Raton, Florida, 2003).

[87] Comsol AB, www.comsol.com. Comsol Multiphysics is formerly known as Femlab.

[88] TIMOSHENKO, S. AND WOINOWSKY-KRIEGER, S., *Theory of plates and shells* (McGraw–Hill, New York, 1959), 2nd ed.

[89] JEN, S. U., YU, C. C., LIU, C. H., AND LEE, G. Y., *Piezoresistance and electrical resistivity of Pd, Au, and Cu films*. Thin Solid Films **434** (2003) 316–322.

[90] BARDEEN, J. AND SHOCKLEY, W., *Deformation potentials and mobilities in nonpolar crystals*. Phys. Rev. **80** (1950) 72–80.

[91] VION, D., AASSIME, A., COTTET, A., JOYEZ, P., POTHIER, H., URBINA, C., ESTEVE, D., AND DEVORET, M. H., *Manipulating the quantum state of an electrical circuit*. Science **296** (2002) 886–889.

[92] PEKOLA, J. P., NIEMINEN, T. E., MESCHKE, M., KIVIOJA, J. M., NISKANEN, A. O., AND VARTIAINEN, J. J., *Shot-noise-driven escape in hysteretic Josephson junctions*. Phys. Rev. Lett. **95** (2005) 197004.

[93] SIMMONDS, R., LANG, K., HITE, D. A., NAM, S., PAPPAS, D. P., AND MARTINIS, J. M., *Decoherence in Josephson phase qubits from junction resonators*. Phys. Rev. Lett. **93** (2004) 077003.

[94] NAIK, A., BUU, O., LAHAYE, M. D., ARMOUR, A. D., CLERK, A. A., BLENCOWE, M. P., AND SCHWAB, K. C., *Cooling a nanomechanical resonator with quantum back–action*. Nature **443** (2006) 193–196.

[95] TEUFEL, J. D., REGAL, C. A., AND LEHNERT, K. W., *Prospects for cooling nanomechanical motion by coupling to a superconducting microwave resonator*. New J. Phys. **10** (2008) 095002.

Appendix A

Derivation of current through NIS junction at weak Coulomb blockade limit

The tunneling rates through NIS junction can be written in the form, as presented in chapter 3

$$\Gamma^{i,+} = \frac{1}{e^2 R_T}\int_{-\infty}^{\infty} n_S(E) f_S(E)\left[1 - f_N(E - E_n^{i,+})\right] \mathrm{d}E \tag{A.1}$$

$$\Gamma^{i,-} = \frac{1}{e^2 R_T}\int_{-\infty}^{\infty} n_S(E) f_N(E - E_n^{i,-})\left[1 - f_S(E)\right] \mathrm{d}E\,, \tag{A.2}$$

where $E_n^{i,\pm} = \pm 2E_C(n + n_G \pm 0.5) \pm eV_i$ and $i = \{L, R\}$. By substituting E_n into the Fermi–function, we obtain

$$f(E \mp E^{i,\pm}) = f(E - 2E_C(n + n_G \pm 0.5) - eV_i) = \frac{1}{1 + \exp\left(\frac{E - eV_i}{k_B T}\right)\exp(-u^{\pm})}\,, \tag{A.3}$$

where $u^{\pm} \equiv 2E_C(n + n_G \pm 0.5)/(k_B T)$. Now at the weak Coulomb blockade limit $E_C \ll k_B T$ and therefore $u^{\pm} \ll 1$, resulting in next to the leading order expansion of the Fermi–function with respect to $u^{\pm}$

$$\begin{aligned} f(E \mp E^{i,\pm}) &\approx f(u=0) + \left.\frac{\mathrm{d}f}{\mathrm{d}u}\right|_{u=0} u^{\pm} \\ &= f(E - eV_i) + \frac{\exp\left(\frac{E - eV_i}{k_B T}\right)}{\left[1 + \exp\left(\frac{E - eV_i}{k_B T}\right)\right]^2} u^{\pm}\,. \end{aligned} \tag{A.4}$$

By denoting $v_i \equiv (E - eV_i)/(k_B T)$ and using the relation $\cosh^2(v/2) = (cosh(v)+1)/2$ leads to

$$f(E \mp E^{i,\pm}) = f(k_B T v_i) + \frac{u^{\pm}}{4\cosh^2(v_i/2)} \,. \tag{A.5}$$

Tunneling rates in Eqs. (A.1) and (A.2) take the form

$$\Gamma^{i,+} = \Gamma_0^{i,+} - \frac{u^+}{4e^2 R_T} \int_{-\infty}^{\infty} \frac{n_S(E) f_S(E)}{\cosh^2\left(\frac{E - eV_i}{2k_B T}\right)} \mathrm{d}E \tag{A.6}$$

$$\Gamma^{i,-} = \Gamma_0^{i,-} + \frac{u^-}{4e^2 R_T} \int_{-\infty}^{\infty} \frac{n_S(E)[1 - f_S(E)]}{\cosh^2\left(\frac{E - eV_i}{2k_B T}\right)} \mathrm{d}E \,, \tag{A.7}$$

where $\Gamma_0^{i,-}$ are the tunneling rates without charging energy, i.e. $E_C = 0$. The tunneling current can be calculated by the above relation according to Eq. (3.5). By substituting $u^{\pm}$, the tunneling current results

$$\begin{aligned} I &= -e \sum_{n=-\infty}^{\infty} P(n) \left[\Gamma^{+,i} - \Gamma^{-,i}\right] \qquad (A.8) \\ &= -e \left[\Gamma_0^{L,+} - \Gamma_0^{L,-} - \frac{\alpha(-V) E_C}{2k_B T e^2 R_T}\left(n_G + \frac{1}{2}\right) - \frac{\alpha(V) E_C}{2k_B T e^2 R_T}\left(n_G - \frac{1}{2}\right)\right] \sum_{n=-\infty}^{\infty} P(n) \\ &\quad + e \left[\frac{\alpha(-V) E_C}{2k_B T e^2 R_T} + \frac{\alpha(V) E_C}{2k_B T e^2 R_T}\right] \sum_{n=-\infty}^{\infty} n P(n) \,, \end{aligned}$$

where

$$\alpha(\pm V) \equiv \int_{-\infty}^{\infty} \frac{n_S(E) f_S(E)}{\cosh^2\left(\frac{E \pm eV/2}{2k_B T}\right)} \mathrm{d}E \,. \tag{A.9}$$

Because of the normalization condition for the probability distribution $\sum_{n=-\infty}^{\infty} P(n) = 1$ and symmetry of the distribution $\sum_{n=-\infty}^{\infty} n P(n) = 0$. The tunneling current in the weak Coulomb blockade limit results in

$$I = I_{E_C=0} + n_G \frac{E_C}{2k_B T e R_T}[\alpha(V) + \alpha(-V)] - \frac{E_C}{4k_B T e R_T}[\alpha(V) - \alpha(-V)] \,. \tag{A.10}$$